Techno-economic analysis of catalytic methane pyrolysis in a fluidized bed reactor with reactor-scale catalyst deactivation modeling

Tamarona, P. B.; Nijssen, T. M.J.; Vlugt, T. J.H.; Ramdin, M.

DOI
10.1016/j.cej.2025.167134

Publication date
2025

Document Version
Final published version

Published in
Chemical Engineering Journal

Chemical Engineering Journal 522 (2025) 167134

Contents lists available at ScienceDirect

Chemical Engineering Journal

journal homepage: www.elsevier.com/locate/cej

Techno-economic analysis of catalytic methane pyrolysis in a fluidized bed reactor with reactor-scale catalyst deactivation modeling

P.B. Tamarona, T.M.J. Nijssen, T.J.H. Vlugt, M. Ramdin *

Process and Energy, Delft University of Technology, Leeghwaterstraat 39, Delft, 2628 CB, The Netherlands

ARTICLE INFO

Dataset link: https://github.com/pbtamarona/methanepyrolysis

Keywords:
Catalytic methane pyrolysis
Fluidized bed reactor
Hydrogen production
Solid carbon byproduct
Techno-economic analysis
Reactor modeling
Catalyst deactivation

ABSTRACT

Methane pyrolysis is a promising route for low-emission hydrogen (H_2) production, with solid carbon as a potentially valuable byproduct. Despite this potential, the economic feasibility of Catalytic Methane Pyrolysis (CMP) with fluidized bed reactors (FBR) has been insufficiently studied. This study develops a conceptual CMP plant using two novel isothermal reactor models—based on continuous stirred-tank reactor (CSTR) and plug-flow reactor (PFR) assumptions—to represent the operational extremes of FBRs. Our reactor models incorporate reaction and catalyst deactivation kinetics from experiments with nickel-supported catalysts, and the framework enables process simulations that account for the catalyst rate required to sustain reactor activity. These models address the lack of proper reduced-order FBR models and the reliance on oversimplified assumptions in the literature. In the baseline scenario, the conceptual plant yields an LCOH ranging from $3.89 to $4.79 per kilogram, defining the expected cost bounds for an FBR-based CMP plant. At a H_2 selling price of $5.00 per kilogram, the process achieves favorable payback time and net present value. Monte Carlo and sensitivity analyses indicate that CMP remains cost-competitive under economic uncertainties. Increased carbon sales could make CMP more economical than steam methane reforming, while unsold byproducts may incur costly sequestration. Reactor heating assessment shows methane combustion with carbon capture minimizes both cost and emissions. Overall, this work demonstrates the economic potential of CMP for H_2 production and provides a practical modeling framework for process evaluation.

1. Introduction

Human-induced climate change, driven by greenhouse gases like carbon dioxide (CO_2) and methane (CH_4), is among the most pressing challenges of the 21st century [1,2]. As countries strive to transition to a low-carbon economy, hydrogen (H_2) has emerged as a pivotal energy carrier due to its versatility and potential to decarbonize various sectors [3,4]. The predominant method of H_2 production, steam methane reforming (SMR), generates significant CO_2 emissions, undermining its environmental benefits [4,5]. While integrating CO_2 capture and storage (CCS) with SMR can mitigate emissions, it reduces energy efficiency, increases costs, and is limited by the availability of suitable geological formations for CO_2 storage [5,6]. Water electrolysis offers a pathway to truly green H_2, yet its high costs and reliance on renewable electricity infrastructure remain barriers to widespread adoption [4–8]. In this context, methane pyrolysis (MP) emerges as a promising bridge technology, producing H_2 and functional solid carbon (C) with low CO_2 emissions while leveraging existing natural gas (NG) resources and infrastructure [6–8]. Although its long-term sustainability is limited by NG depletion, MP offers significant potential as a transitional solution toward a sustainable economy [6].

MP is the thermal decomposition process of CH_4 into gaseous H_2 and solid C, as shown below [8–10]:

$$CH_4(g) \rightleftharpoons C(s) + 2\,H_2(g); \quad \Delta H_{298\,K} = 74.52\,kJ\,mol^{-1}. \tag{1}$$

As this reaction is endothermic, higher temperatures are favorable, requiring 900 °C to 1200 °C without a catalyst for significant H_2 yield [5,6,11]. Various solid catalysts (both metal- and C-based) have been developed to enhance the conversion rate at lower reaction temperatures [4–8,11,12]. A lower temperature can be beneficial as it reduces energy consumption, minimizes material stress, and enables a safer process. Catalysts can also improve the type and quality of the solid C produced [4,13]. However, the carbon produced in catalytic methane pyrolysis (CMP) often deposits on the active sites of solid catalysts, leading to catalysts encapsulation and subsequent deactivation. In fixed-bed reactors, this leads to an increased pressure drop and eventually blockage of the gas flow, significantly restricting its applicability in industrial settings [6].

* Corresponding author.
E-mail address: m.ramdin@tudelft.nl (M. Ramdin).

https://doi.org/10.1016/j.cej.2025.167134
Received 28 May 2025; Received in revised form 28 July 2025; Accepted 10 August 2025
Available online 19 August 2025

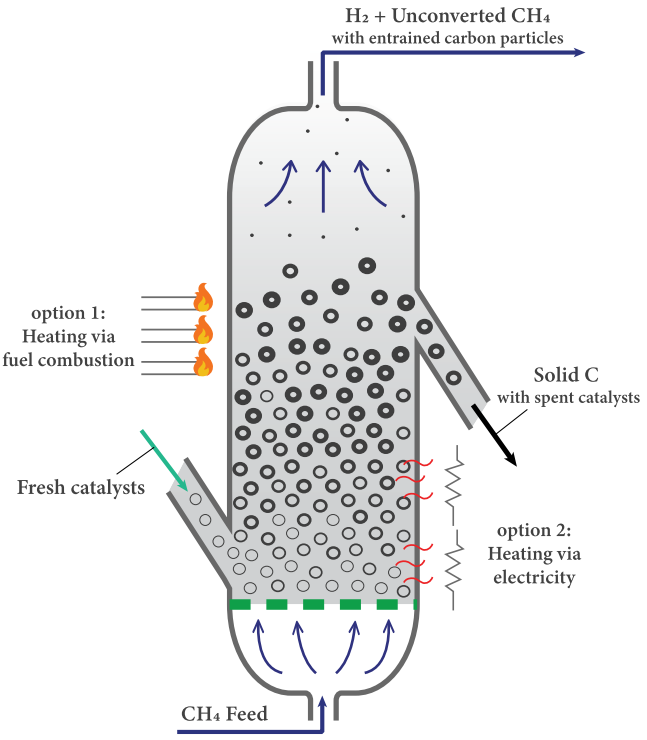

Fig. 1. Schematic representation of a continuous CMP FBR concept: CH_4 is introduced from the bottom of the reactor. The H_2 product and unreacted CH_4 are collected at the top. Fresh catalyst is continuously fed into the reactor from a side inlet near the base. Solid C products and spent catalyst are discharged through a side outlet positioned slightly above the bed height when initially fluidized. The TEA in this study explores various reactor heating methods, such as fuel combustion (CH_4 and H_2) and electricity.

A fluidized-bed reactor (FBR) is a potential solution to this issue through a modification of its conventional design: continuous addition of fresh catalyst and simultaneous removal of spent catalyst along with the produced carbon [4,6,7,11,12]. The vigorous motion of particles in FBRs enhances heat and mass transfer between the gas and the solid catalyst. As a result, temperature control is improved, and the formation of hot spots is prevented. Fig. 1 illustrates a potential FBR configuration for an industrial CMP process. This design was influenced by the elutriation of particles [14]. The encapsulation of the metal catalyst by the carbon material reduces the particle density [15–17], allowing the carbon product and spent catalysts to be carried upward by the gas flow and expelled from the reactor [4,12]. FBR is a promising technology for CMP, however, several challenges and limitations still need to be addressed [4]. These challenges include overcoming the complexities of reactor design and operation, developing a cost-effective catalyst with high activity and a long lifespan, potentially with the ability to be regenerated, and addressing both the prevention and mitigation of solid carbon agglomeration. Numerous experimental studies, computational analyses, and proof-of-concept investigations on CMP in FBRs have been reported in recent literature [15,16,18–23]. Despite its potential, to the best of the knowledge of the authors, only two studies in the current literature have explored the economic feasibility of CMP in FBRs at an industrial scale [14,24]. This contrasts with the comparatively larger number of techno-economic studies available for alternative MP reactors, such as molten metal and molten salt reactors [5,25–30]. While molten metal and salt reactors show promise, significant challenges remain, including the stability of the molten medium and corrosion at high operating temperatures (above 900 °C to 1000 °C), particularly in steel-based reactor designs [6].

Zhang et al. [24] studied the CO_2 mitigation costs associated with CMP with FBR for H_2 production and subsequent power generation in a fuel cell. The study estimate a profitable levelized cost of electricity of €177/MWh of CMP with Ni-based catalyst. However, the analysis assumed perfect catalyst separation and recycling, without evaluating the necessary solid handling processes. In addition, the relationship between catalyst flow rate, deactivation, and reactor conditions – key factors in estimating variable production costs – was oversimplified by fixing the ratio of deposited carbon to the catalyst mass inside the reactor. In a more recent work, Riley et al. [14] studied the techno-economic performance of a 216 tonnes per day (TPD) conceptual CMP plant using a FBR. The authors estimated the levelized cost of H_2 (LCOH) to be less than $\$3.25\,kg^{-1}$, assuming a NG price of $7/MMBtu and a catalyst cost of $\$8\,kg^{-1}$, without accounting for the sales of the solid C. Details of the reactor model used to determine the relationship between catalyst rate and operating conditions were not reported. Both Zhang et al. [24] and Riley et al. [14] assumed a simple first-order kinetics, neglecting chemical equilibrium and reverse reactions, which can lead to unrealistic calculations. Riley et al. [14] reported a single-pass CH_4 conversion of up to 99% at operating conditions of 700 °C and 9.2 bar. This is significantly higher than the equilibrium conversion, which is approximately 42% at these conditions, as indicated by the equilibrium CH_4 conversion curves, shown in Figure S.10 of the supporting information (SI).

A computational fluid dynamics – discrete element method – multi-grain model study on FBR for CMP shows that the continuous introduction and removal of catalyst particles in the reactor lead to a stable average deactivation factor of the particles [21]. Based on this idea, our study introduces simplified yet practical, novel steady-state FBR models to determine the catalyst rate required to maintain a specified reactor activity. These models are integrated with Aspen Plus simulations of the conceptual plant proposed in this work, enabling overall plant simulation while accounting for the interplay of the reactor conditions, reaction kinetics, catalyst rate and deactivation. The reaction kinetics are adopted from the experimental work of CMP with Ni-based catalyst of Hadian et al. [17], which incorporate equilibrium considerations, adsorption–desorption processes, and catalyst deactivation over time. The reactor models, implemented in Python, are fully accessible in the Data availability section, ensuring reproducibility and allowing modifications for evaluating other plant configurations, reactor designs, CMP catalysts, and kinetic models for further studies.

The reactor and process plant models serve as the basis for the economic evaluation of CMP for large-scale H_2 production, with solid carbon as a byproduct. In our study, key investment parameters, including the LCOH, net present value (NPV), and payback time (PBT), were estimated. Using similar price assumptions as in Riley et al. [14], at a reactor temperature of 700 °C and pressure of 1.12 bar, our simulation yields an average LCOH of $\$4.86\,kg^{-1}$, significantly higher than what was predicted by Riley et al. [14]. This discrepancy highlights the importance of accurate kinetic and reactor modeling. In our baseline scenario, the LCOH ranges from $3.89 to $4.79 per kg. Based on an H_2 selling price of $\$5\,kg^{-1}$, the estimated PBT and NPV from average simulation conditions are 4.7 years and $102.3 million, respectively. Our monte Carlo sensitivity analysis indicates that CMP remains cost-competitive despite economic uncertainties. Further analyses identify reactor temperature, CH_4 price, solid C sales, and disposal fees as critical parameters to the process economics. Scaling analysis shows substantial cost reductions as H_2 production scales from 12.5 TPD to 800 TPD and predicts an unprecedented capital cost-scaling curve for CMP plants. We also evaluate the economic and CO_2 emission impacts of reactor heating methods, including electrical heating, are evaluated. The results show that using CH_4 combustion with CCS for heating achieves a low production cost with minimal emissions, whereas H_2 combustion incurs the highest cost. Electric heating powered by grid electricity leads to the highest emissions.

This research aims to address the gap in the literature regarding an extensive techno-economic analysis (TEA) of large-scale CMP with FBR. The paper is structured as follows: **Catalyst and reaction kinetics** -

introduces the significance of catalysts in MP and the reaction kinetics for Ni-based catalyst. **Reactor modeling** - describes the development of the simplified CMP reactor models. **Conceptual plant and process simulation** - describes the conceptual plant design and its integration with the reactor models. **Techno-economic analysis** - presents the TEA framework, key assumptions, and financial metrics. **Results and discussions** - discusses the results, focusing on reactor performance, economic feasibility, and sensitivity analyses. The paper concludes with a summary of our main findings, remarks and recommendations.

2. Catalyst and reaction kinetics

Catalysts play a crucial role in enhancing the efficiency of the CMP process by reducing the reaction temperature required to achieve sufficient conversion. The type and quality of the solid C byproduct formed during CMP are significantly influenced by the choice of catalyst [4,13]. CMP with C-based catalyst [31–34] and non-catalytic MP [35–38] typically produce carbon co-product in the form of amorphous carbon or graphite. Metal-based catalysts, particularly those containing transition metals such as nickel (Ni), iron (Fe), and cobalt (Co), tend to produce filamentous carbon such as carbon nanotube (CNT) and nanofiber (CNF) from CMP [4–7,11,12]. CNTs and CNFs have a wide range of applications, with prices varying significantly from as low as $\$25\,kg^{-1}$ to as high as $\$600\,000\,kg^{-1}$, depending on product characteristics, purity, and application requirements [39]. The high value and versatility of these materials could add substantial economic benefits to the CMP process.

Ni-based catalysts exhibit higher activity compared to Co-, Fe-, molybdenum-, and C-based catalysts [4]. These catalysts operate effectively at relatively low temperatures, as low as 500 °C, whereas Fe-based catalysts typically require temperatures higher than 700 °C. Despite the superior activity and low-temperature operation of Ni-based catalysts, rapid deactivation occurs at temperatures above 600 °C due to carbon deposition and sintering. To overcome this challenge, one of the commonly implemented strategies is to combine Ni with other materials, such as Fe, bismuth (Bi), or potassium (K), and add support to increase stability [40]. The addition of supports, which are usually metal oxides (i.e., Al_2O_3, MgO, and SiO_2), changes the pore structure, surface area, and catalyst composition, which affects the activity and stability of the overall catalyst [41].

Various kinetic studies on CMP with metallic catalysts are documented in the literature [17,42–53]. These studies show that the actual reaction rate of CMP decreases over time due to carbon accumulation at the catalyst surface, leading to catalyst deactivation. The reaction rate as a function of time, $r(t)$, can be expressed as [17,49–53]:

$$r(t) = r_0 \cdot a(t), \tag{2}$$

where r_0 represents the initial reaction rate and $a(t)$ denotes the time-dependent deactivation factor.

Several studies proposed a mechanism for CMP involving the molecular adsorption of CH_4, followed by stepwise dehydrogenation reactions until separate adsorbed carbon atoms and H_2 molecules are obtained [48,51,54–56]. In this scheme, the first dehydrogenation step – an initial reaction in which a hydrogen atom is removed from an adsorbed CH_4 molecule, resulting in the formation of an adsorbed methyl radical (CH_3) and a hydrogen atom – is considered the rate-limiting step of the overall process. Based on this mechanism Amin et al. [51], derived the following equation to describe the initial reaction rate of CH_4 decomposition:

$$r_0 = \frac{k\left(P_{CH_4} - P_{H_2}^2/K_p\right)}{\left(1 + K_{CH_4}P_{CH_4} + K_{H_2}P_{H_2}^{1.5}\right)^2}, \tag{3}$$

where k is the specific reaction rate constant, K_p is the equilibrium constant of Eq. (1), K_{CH_4} and K_{H_2} are the overall adsorption constants for CH_4 and H_2, respectively. The terms P_{CH_4} and P_{H_2} are the partial pressures of CH_4 and H_2, respectively.

Table 1
Initial reaction rate and deactivation factor parameters.
Source: Adapted from Hadian et al. [17].

Constant	Parameter	Value	Unit
k	A	9.77054	$mol_{CH_4}(Pa\ kg\ s)^{-1}$
	E	88	kJ mol^{-1}
K_{CH_4}	A_{CH_4}	6.887737e−10	Pa^{-1}
	ΔH_{CH_4}	−56	kJ mol^{-1}
K_{H_2}	A_{H_2}	5.8009466e−16	Pa$^{-1.5}$
	ΔH_{H_2}	−144	kJ mol^{-1}
k_d	A_d	18.39	s^{-1}
	E_d	147	kJ mol^{-1}
$k_{d,C}$	$A_{d,C}$	309.87	
	$\Delta H_{d,C}$	−26	kJ mol^{-1}
k_{d,CH_4}	A_{d,CH_4}	−4.431483e−3	Pa^{-1}
	$\Delta H_{d,CH_4}$	−5.376	kJ mol^{-1}
k_{d,H_2}	A_{d,H_2}	−2.44388e−05	Pa$^{-0.83}$
	$\Delta H_{d,H_2}$	−80.19	kJ mol^{-1}

Amin et al. [51] also proposed a semi-empirical equation for the catalyst deactivation factor, derived from a species balance on the active sites of the catalyst:

$$a(t) = \left(1 - 0.5 \cdot k_d \cdot t \cdot \left(k_{d,C} + k_{d,CH_4}P_{CH_4} + k_{d,H_2}P_{H_2}^{0.83}\right)\right)^{0.8}, \tag{4}$$

where t is time, and k_d, $k_{d,C}$, k_{d,CH_4}, and k_{d,H_2} are the constants.

Building upon these models, Hadian et al. [17] studied CMP kinetics using Ni-based catalyst supported on silica in a lab-scale FBR. From the experimental results, the kinetics and deactivation constants were estimated for the temperature range of 550 °C to 600 °C with error margins of 10% for the initial reaction rate and 17% for the deactivation factors. The parameter values are listed in Table 1, which serves as the basis for the reaction kinetics in the reactor models developed in this work. The initial reaction rate constant, k, and deactivation constant, k_d, are described in Arrhenius form—$k = A \cdot \exp\left(-\frac{E_a}{RT}\right)$. Meanwhile, K_{CH_4}, K_{H_2}, $k_{d,C}$, k_{d,CH_4}, and k_{d,H_2} follow the Van 't Hoff equation—$K = A \cdot \exp\left(-\frac{\Delta H}{RT}\right)$. Here, A, E_a, ΔH and R are the pre-exponential factor, the activation energy, the heat of adsorption and the universal gas constant, respectively. The equilibrium constant, K_p, which dictates the driving force of the reaction, forward or backward, to ensure that the expression of the rate adheres to the equilibrium constraints, is calculated following the approach proposed by Zavarukhin and Kuvshinov [49],Kuvshinov et al. [57]:

$$K_p = 5.088 \cdot 10^{10}\ \text{Pa} \cdot \exp\left(-\frac{91.2\ \text{kJ mol}^{-1}}{RT}\right) \tag{5}$$

It is important to note that both Amin et al. [51] and Hadian et al. [17] conducted experiments using laboratory-scale reactors at atmospheric pressure. The reported deactivation parameter values seems to be valid only at conditions near atmospheric pressure, as the model predicts activity larger than 1 for H_2 partial pressures of ±1 bar. Accordingly, this study limits the reactor pressure of the conceptual plant to 1.12 bar, a constraint with cost implications discussed in Results and discussions. This underscores the need for further investigation into the kinetics of CMP at elevated pressures.

3. Reactor modeling

The reactor models developed in this work are essential for accounting for the interplay between reactor operating conditions (e.g., pressure, temperature, etc.), catalyst feed/extract rates, reaction kinetics and catalyst deactivation. These models were implemented in Python and integrated with the Aspen Plus process simulation since there are no built-in reactor models in Aspen Plus that account for all these factors comprehensively.

In this study, we present two simplified models of the complex CMP fluidized bed concept. These models omit the detailed flow and fluidization behaviors of the solid and gas phases within the FBR unit. Instead, the models represent two operational extremes of fluidized bed behavior: one in which both the solid and gas phases are well mixed, and another in which both phases approximate plug-flow behavior. Thus, steady-state reactor models were developed based on ideal reactor assumptions: the continuous stirred-tank reactor (CSTR) and the plug-flow reactor (PFR). The CSTR model simulates a fully turbulent FBR, where solids are perfectly mixed, and the violent agitation of the bed causes significant back-mixing of the gas phase [58]. This scenario is typically observed in FBR with low height-to-diameter ratios [59]. The PFR model simulates a *transport* FBR, where the gas velocity is high enough to entrain solids, causing the solids to flow along the length of the reactor with the gas [58]. It is important to note that the solid and gas velocities may differ. The PFR model also describes a type of CMP fluidized bed in which solids move due to particle expansion from the accumulation of solid C and the constant injection of fresh catalyst particles. This configuration is typical in reactors with high height-to-diameter ratios, where axial mixing is limited. An example of such a reactor is the bench-scale FBR system for continuous CMP presented by Bae et al. [15]. We propose that the implementation of these two idealized reactor models in the process simulations defines the upper and lower bounds of the techno-economic performance of the conceptual CMP plant. The goal of the TEA in this study is not necessarily to provide a definitive figure for final investment decisions, but rather to offer insights for creating long-term strategies, facilitate comparison with other processes, and encourage further research.

Both reactor models assume isothermal conditions, with constant external heat input supplied to maintain reactor temperature. The Python implementation of both CSTR and PFR model, along with the documentations, are available in the Data availability section.

3.1. Continuous stirred-tank reactor

Fig. 2 illustrates the isothermal fluidized bed CSTR analysis proposed in this work. The gas species concentrations inside the reactor, represented by the partial pressures, are assumed to be uniform and equal to those of the products exiting the reactor [60]. The solid particles, consisting of the catalyst and solid C, are assumed to be well-mixed throughout the reactor. The proposed model employs mass balance equations for the reactants to determine the outlet flow rates of the reactor, as expressed as follows:

$$F_{\mathrm{CH_4,out}} = F_{\mathrm{CH_4,in}} - r \cdot W_{\mathrm{cat}}, \tag{6}$$

$$F_{\mathrm{H_2,out}} = F_{\mathrm{H_2,in}} + 2 \cdot r \cdot W_{\mathrm{cat}}, \tag{7}$$

where $F_{\mathrm{CH_4,in}}$ and $F_{\mathrm{CH_4,out}}$ are the inlet and outlet mole flow rates of CH_4, respectively, while $F_{\mathrm{H_2,in}}$ and $F_{\mathrm{H_2,out}}$ are those of H_2; r is the reaction rate, and W_{cat} is the catalyst holdup. These equations are solved through an iterative process that adjusts initial outlet mole flow guesses, for calculating the reaction rate, to minimize the residuals of the molar balances. This is implemented using the `minimize` function from the SciPy library [61], with an objective function defined as the sum of squared molar balance residuals for CH_4 and H_2. For steady-state condition, the reaction rate in the reactor, r, is calculated as:

$$r = r_0 \cdot \bar{a}. \tag{8}$$

where r_0 is the initial reaction rate, defined in Eq. (3), and $\bar{a}$ is the average catalyst deactivation factor inside the reactor.

The average deactivation factor is derived by integrating the catalyst deactivation profile over the particle residence time distribution (RTD). The RTD describes the residence time of particles within the reactor, providing insights into its mixing characteristics [60]. The average deactivation factor computed numerically using the following equation:

$$\bar{a} = \sum_i f_i \cdot a(t_i), \tag{9}$$

where f_i is fraction of particles in the reactor with residence times of t_i and $a(t_i)$ represents the deactivation factor for particles with residence time of t_i calculated using Eq. (4). The fraction of particles exiting within discrete time intervals is computed using the differences between evaluations of cumulative distribution function, $F(t)$. For an ideal CSTR, the cumulative distribution function, representing the fraction of the material that has been in the reactor at time t or less, is expressed as [60]:

$$F(t) = \int_0^t \frac{e^{-t/\tau}}{\tau} = 1 - e^{-t/\tau}, \tag{10}$$

where τ is the average residence time, defined as $W_{\mathrm{cat}}/m_{\mathrm{cat}}$, with m_{cat} being the catalyst mass flow rate. The model cuts off the calculation of $F(t)$ for evaluating the RTD when 99.9% of the particles have exited the reactor.

In this study, the average deactivation factor of the reactor, $\bar{a}$, is maintained at a target value specified as a user input. The catalyst mass flow rate, m_{cat}, is adjusted iteratively, with recalculations of average residence time, reaction kinetics, and mass balances using the reactor model, until the difference between the computed and target deactivation falls within 0.001. After achieving convergence, the outlet mole flow rates is computed based on the final catalyst mass flow rate obtained from the iteration.

3.2. Plug-flow reactor model

Fig. 3 illustrates the proposed isothermal fluidized bed PFR model. PFRs operate with a continuous change in reaction conditions along the reactor length [60]. As CH_4 and H_2 flow through the reactor, the concentrations of each component change progressively. Unlike the CSTR model where the catalyst is well-mixed throughout the reactor volume, the PFR model assumes catalyst movement along the gas flow direction, with lower velocity, no axial mixing, and complete radial uniformity. The catalyst movement results from the elutriation of material and the continuous injection of fresh catalyst at the bottom part of the reactor. As the catalyst flows vertically along the height of the reactor, it gradually deactivates due to carbon accumulation, affecting its activity as a function of time.

The PFR analysis is performed by discretizing the length of the reactor into finite segments with equal amount of catalysts and treated like an individual CSTR unit. The reaction kinetics and catalyst deactivation changes along the reactor length. The model calculates the flow rates of CH_4 and H_2 at each segment, solving for the outlet conditions of the reactor by progressing from the inlet (first segment) to the outlet (last segment). The mass balance equations for a PFR segment are:

$$F_{\mathrm{CH_4,in}}(i+1) = F_{\mathrm{CH_4,in}}(i) - r(i) \cdot \frac{W_{\mathrm{cat}}}{n}, \tag{11}$$

$$F_{\mathrm{H_2,in}}(i+1) = F_{\mathrm{H_2,in}}(i) + 2 \cdot r(i) \cdot \frac{W_{\mathrm{cat}}}{n}, \tag{12}$$

where $F_{\mathrm{CH_4,in}}(i)$ and $F_{\mathrm{H_2,in}}(i)$ are the inlet mole flow rates of CH_4 and H_2 for segment i, $r(i)$ is the reaction rate in segment i, and n is the number of segments. As in the CSTR model, the mass balance equations are solved by iteratively adjusting outlet flow rates to minimize molar balance residuals for CH_4 and H_2.

The catalyst deactivation is assumed to remain constant and uniform within each segment and is modeled as a function of the axial length of the reactor. The reaction rate at a given segment of the reactor, $r(i)$, is then expressed as:

$$r(i) = r_0(i) \cdot a(i), \tag{13}$$

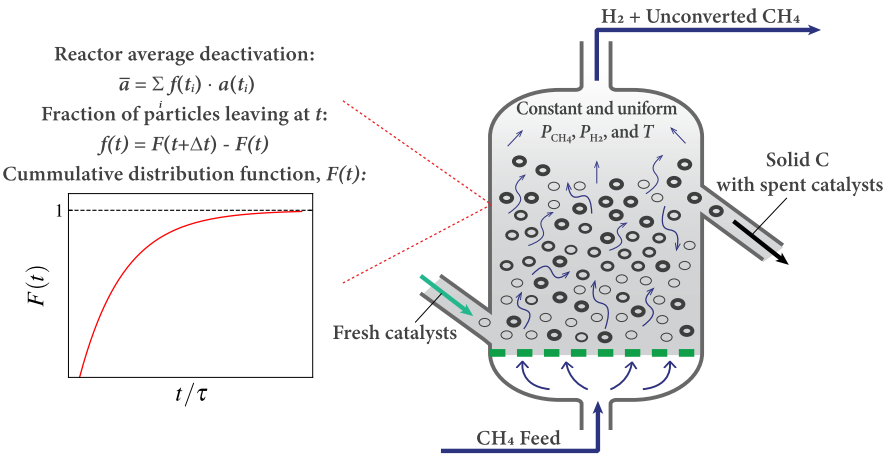

Fig. 2. Schematic representation of the steady-state isothermal fluidized bed CSTR model, assuming uniform species concentrations and well-mixed catalysts throughout the reactor. The model uses mass balances and reaction kinetics to solve for the outlet flow rates—Eqs. (6) to (8). The kinetics account for the average catalyst deactivation, $\bar{a}$, calculated by weighting the deactivation at different times with the fraction of particles leaving at those times, $f(t)$ – Eq. (9). The fraction of particles exiting at a given time is determined by the change in the cumulative distribution function, $F(t)$, over a small time interval – Eq. (10).

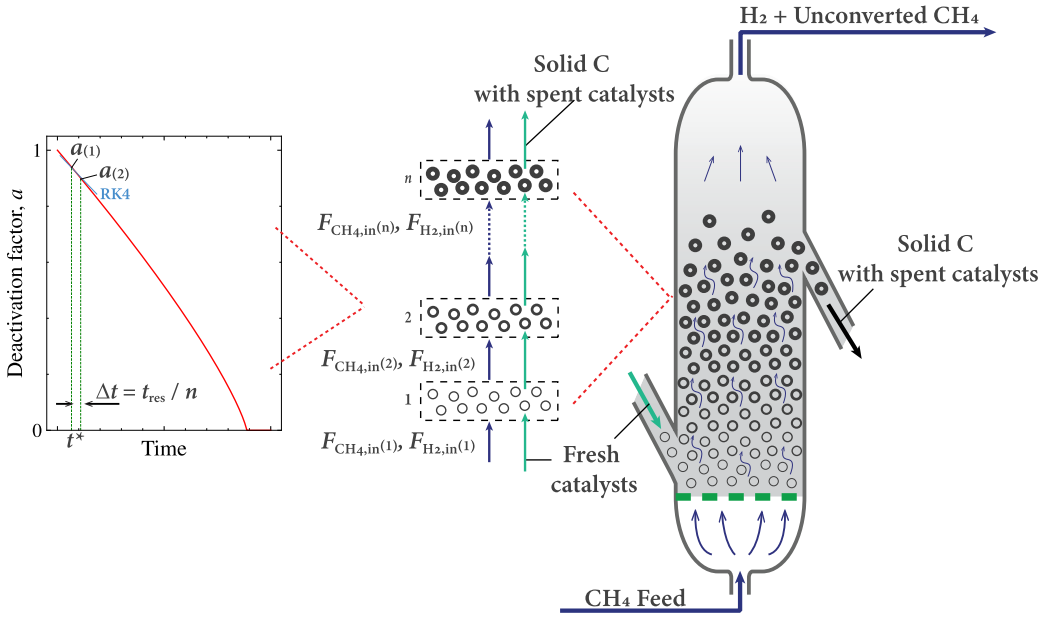

Fig. 3. Schematic representation of the steady-state isothermal fluidized bed PFR model. The reactor is analyzed by discretizing the axial length into segments. Mass balances, reaction kinetics, and deactivation are computed sequentially to determine the outlet conditions—Eqs. (11) to (14). The inlet mole flow rates of CH_4 and H_2 of each segment are denoted as $F_{CH_4,in}(i)$ and $F_{H_2,in}(i)$, respectively, continuously changes as the gas progresses along the reactor length. Catalyst particles are assumed to flow vertically with the gas stream, progressively deactivating due to carbon accumulation.

where $r_0(i)$ is the initial reaction rate at segment i, computed using Eq. (3), while $a(i)$ is the catalyst activity at segment i. The catalyst deactivates gradually at each segment from entering and exiting the reactor. At the first segment, upon entering the reactor, the deactivation factor of the catalyst particles is calculated using Eq. (4), with the time variable evaluated as the time the particles spent in each segment, which is calculated as:

$$\Delta t = \frac{t_{res}}{n} = \frac{W_{cat}/m_{cat}}{n}, \tag{14}$$

where t_{res} is the residence time of the catalyst particles and n is the total number of segments. For the second and subsequent segments, the catalyst deactivation value is approximated using the fourth-order Runge–Kutta (RK4) method for first-order linear ordinary differential equations [62]. This approximation is evaluated at time t^*, an intermediate variable representing the time required for catalyst particles to deactivate up to the deactivation value of the previous segment when exposed to $P_{CH_4}(i)$ and $P_{H_2}(i)$. Time t^* is solved using `root scalar` function from SciPy [61]. The calculations for mass balances, reaction kinetics, and deactivation factors are performed sequentially for each segment by the model until the outlet flow rates of the final segment are solved—specifically, the flow rates of species (CH_4, H_2, and solid C) at the reactor exit. Once the deactivation values for all segments are obtained, the average deactivation factor of the catalyst across the reactor can be computed as:

$$\bar{a} = \frac{1}{n}\sum_{i=1}^{n} a(i). \tag{15}$$

Similar to the CSTR analysis, the catalyst rate in this PFR analysis is adjusted iteratively to achieve the specified average catalyst activity,

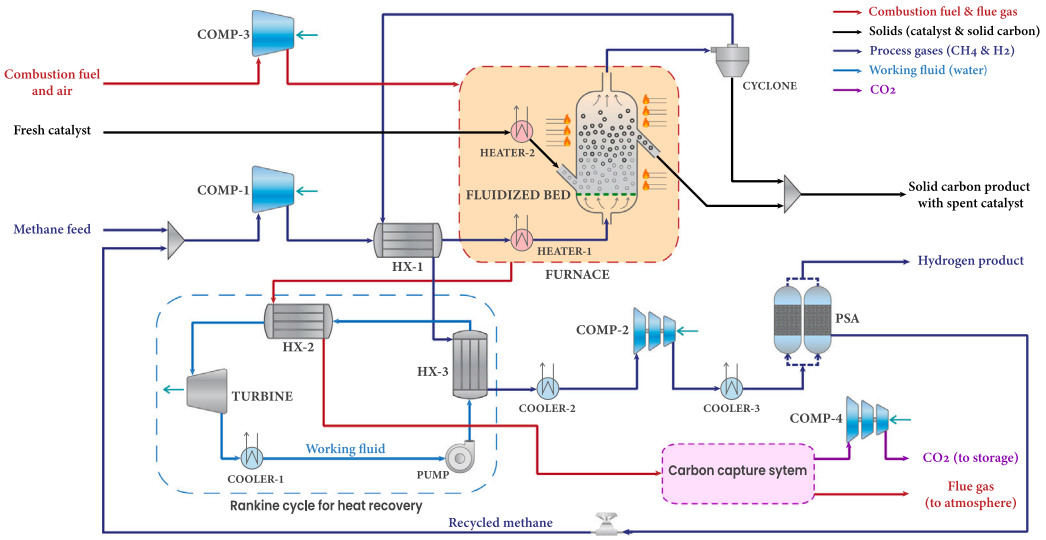

Fig. 4. PFD of the conceptual CMP plant with combustion heating and CCS. CH_4 feed is mixed with the recycle stream, compressed to 1.4 bar by COMP-1, and preheated in HX-1 and HEATER-1 before entering the FBR at 650 °C. Catalysts are preheated in HEATER-2 and fed into the reactor to facilitate the reaction. COMP-3 draws gas-fuel and air for combustion in the furnace, supplying heat to the preheaters and reactor. Gas and solid products are separated in the reactor; gas passes through CYCLONE to remove entrained carbon particles and preheats incoming feed via HX-1, while solid C products are collected. A Rankine cycle system, comprising HX-2, HX-3, TURBINE, COOOLER-1, and PUMP, recovers heat from process and exhaust gases. The process gas is compressed by COMP-2 to the PSA pressure of 15 bar. COOLER-2 and -3 facilitate the compression and adsorption. The PSA purifies the H_2 product, and the CH_4-rich tail gas is recycled back to the process. A CCS system extracts CO_2 from exhaust gas, compressing it to 74 bar via COMP-4 for transport and storage.

$\bar{a}$, along the reactor. Convergence is reached when the average activity matches the desired value within a tolerance of 0.001.

4. Conceptual plant and process simulation

Various large-scale MP conceptual plants have been developed in the literature, with molten reactors being utilized in most designs. This work presents a CMP conceptual plant using FBR with two distinct configurations based on reactor heating methods: fuel combustion (CH_4 and H_2) and electric heating. For plant with CH_4 combustion, there are two plant versions to simulate the process plant with and without CCS integration.

The feedstock is assumed to be 100% pure CH_4, rather than NG or biogas. This is due to the lack of available pyrolysis kinetics data for other components in NG, such as ethane and propane. For biogas, components like CO_2, N_2, H_2O, and H_2S can significantly increase the upstream and downstream separations requirements, reducing process feasibility. To address this, detailed modeling of the gas separation systems for CMP with industrial feedstocks will be conducted in a follow-up study. This study targets a H_2 purity of 99.5%, achieved through a pressure swing adsorption (PSA) unit. PSA has been shown to recover high-purity H_2 from H_2/CH_4 mixtures containing 65%–98% H_2 [63,64], which aligns with the PSA feed composition in our process simulations. The PSA unit is assumed to operate at 15 bar with a maximum recovery of 90%, based on values reported for SMR processes [65–68]. Sensitivity analysis of PSA pressure, presented in Figure S.11 of the SI, demonstrates that it has a relatively small impact on the overall process plant costs.

For the baseline scenario, the H_2 production capacity of the plant is 100 TPD. The compressors are modeled as centrifugal type, while the turbine as condensing-steam (axial) type. The mechanical and isentropic efficiencies for compressors and turbines are assumed to be 0.90 and 0.85, respectively, while pump and driver efficiency is set at 0.90 and 0.85, respectively. The efficiency of the furnace is 0.85 for fuel combustion and 0.90 for electric heating. Pressure drops in heat exchangers, including heaters and coolers, are ignored. The incoming and outgoing temperature of cooling water are 25 °C and 35 °C, respectively. Ambient air is assumed to compose of 79 vol% N_2 and 21 vol% O_2 at 25 °C and 1 atm.

4.1. Plant description

Fig. 4 illustrates the process flow diagram (PFD) of the conceptual CMP process plant with combustion heating and CCS. The process starts with feeding CH_4 to the plant at 1.01 bar and 25 °C. Upon entering the system, the feed is mixed with recycled stream rich in CH_4 (with some traces of H_2). The mixed gas is then compressed by a compressor, COMP-1, to 1.4 bar. This compression ensures adequate gas flow against pressure drops in the FBR. The pressurized CH_4 stream then passes through a heat exchanger, HX-1, where it is preheated using thermal energy recovered from the outlet gas stream of the reactor. HEATER-1 further heats the preheated CH_4 to the reactor operating temperature, while HEATER-2 performs the same function for the fresh catalyst feed. Both preheaters are powered by same heating furnace as the reactor. At the core of the process is the FBR, which operates at a temperature of 650 °C. In the sensitivity analyses, this is varied between 550 °C to 750 °C. The pressure across the reactor ranges from 1.12 bar to 1.4 bar, as the reactor is sized such that the outlet pressure is 1.12 bar. In the FBR, CH_4 undergoes decomposition according to Eq. (1) within the fluidized catalyst bed. Gaseous and solid components are separated by the FBR, as described in Fig. 1. Fine carbon particles may be entrained in the gas flow and exit the reactor through the top. These particles are separated from the gas stream using a cyclone placed downstream of the gas exit of the reactor. After passing through the cyclone, the high temperature gas mixture passes back through HX-1 to preheat the incoming CH_4 feed.

The carbon particles collected from the cyclone and the carbon products along with the spent catalyst from the reactor are gathered for further purification, direct sale, or disposal (sequestration) [69–74]. Spent catalyst may also be separated from the carbon product, then regenerated, and recycled to the reactor [22,75,76]. The separation of the catalyst from the carbon product is critical, as impurities lower the value of the solid C and raise environmental and safety concerns. It also enables catalyst regeneration and recycling without burning off the carbon and emitting CO_2. Various separation methods have been proposed in the literature, including selective oxidation, ultrasonication, acid treatment, and carbon dislodging by vigorous stream [22,69–76]. However, due to limited experimental and kinetic studies, this step

remains difficult to model accurately and is currently being explored in more detail in our follow-up study.

The preheaters and reactor are assumed to be contained within a combustion furnace when heating is via CH_4 or H_2 combustion. Fuels are combusted with O_2 from ambient air, supplied at 5% excess mass flow for stoichiometric combustion. The gas-fuel and air mixture is drawn in by a compressor, COMP-3, as the furnace operates slightly above atmospheric pressure. In this heating mode, the process H_2/CH_4 gas mixture from the reactor is then passes through a heat exchanger, HX-3, to heat a working fluid, water, in a Rankine cycle. Integrating this cycle improves energy efficiency by recovering thermal energy from combustion exhaust gas. The exhaust gas energy is utilized in heat exchanger HX-2 to convert pressurized liquid water at 102 °C into steam at 810 °C. The steam expands in a turbine, which is connected to a generator to produce electrical power. After expansion, the steam is condensed in COOLER-1 and pumped back to HX-3 at 50 bar. Exhaust gas leaving HX-2 are sent to the CCS unit, where CO_2 is captured from the exhaust gas with an assumed capture rate of 90%. The CO_2-lean flue gas is released into the environment, while the captured CO_2 is compressed by COMP-4 to 74 bar for transport and storage [77]. COMP-4 is designed as a three-stage compressor with intercoolers to minimize CO_2 outlet temperature.

When electric heating is used, the Rankine heat recovery cycle and CCS systems are not applicable. Instead, the H_2/CH_4 gas mixture flows directly to heat exchanger COOLER-2 after exiting HX-1. In COOLER-2, the H_2/CH_4 gas mixture is cooled to 30 °C by cooling water before entering compressor COMP-2 to reduce the compression workload. COMP-2 compressed the gas mixture to the PSA operating pressure of 15 bar. As with the CO_2 compressor, COMP-2 is a three-stage compressor with intercoolers to limit temperature increase from compression. At the compressor exit, the gas is reheated due to compression and is subsequently cooled in COOLER-3 to facilitate PSA operation. The PSA unit purifies H_2 to meet stringent product specifications. Meanwhile, unreacted CH_4 and residual H_2 are recovered from the PSA tail gas and recycled back into the process feed. Figure S.2 and S.3 of the SI provide the PFDs of the CMP plant with combustion and electric reactor heating, respectively, with the complete stream annotations. Table S.1–S.6 of the SI provide the stream data of the CMP plants for each reactor heating mode configuration following CSTR and PFR simulations.

4.2. Process simulation

The proposed process concepts are simulated using Aspen Plus Software V12, applying the Peng–Robinson property method [78] to calculate the thermodynamic properties for most of the process streams. For water streams within the Rankine cycle, the Steam-TA property method is used. The stream class MIXCIPSD is configured to ensure accurate modeling of the solid catalyst and solid C streams. In the Aspen Plus simulation, the reactor is modeled using either the built-in PFR or CSTR models, depending on which reactor analysis is being performed. To account for catalyst deactivation due to the solid C growth in the process simulation, the Python-based PFR and CSTR models were integrated to Aspen Plus simulation through iterative calculations. This framework enables comprehensive process plant simulations that consider the extent of reactor deactivation influenced by reactor conditions, reaction kinetics, and catalyst rate. The final results from the Aspen Plus simulation are then used as the basis for the techno-economic analysis (TEA) of the CMP plant. Further details on the simulation workflow, including the Aspen Plus–Python integration, are provided in the SI. The Python routine and Aspen Plus simulation files are available in the Data availability section.

5. Techno-economic analysis

TEA is a critical method for evaluating the economic performance of processes in industries [79]. In this study, TEA is performed to assess the overall value of the conceptual CMP plant described previously, enabling a comparative evaluation of CMP using a fluidized bed against other MP processes and H_2 production methods. The analysis focuses on estimating the capital expenditures (CAPEX), operating expenditures (OPEX), LCOH, NPV and PBT of the plant. This section outlines the parameters, assumptions, and methodologies used to perform these assessments. The subsequent Results and discussions section explores sensitivity analyses to determine the influence of critical variables, such as catalyst cost and carbon sales, on the economic viability of the CMP plant.

5.1. Capital expenditure

The CAPEX estimation in this study is derived based on limited cost data and design detail, and is therefore classified as "Class 4" estimates with accuracy range of ±30% [58]. The purchase cost of major process equipment is estimated using cost correlations from the literature, adjusted to reflect 2023 pricing with the Chemical Engineering Plant Cost Index (CEPCI). Table S.9 of the SI summarizes the cost correlations used in this study. The remaining capital costs are estimated as factors of the equipment cost.

The total cost of designing, constructing, and installing a plant, along with the preparation of the plant site, is referred to as the fixed capital investment (FCI). The FCI comprises the following components: inside battery limits (ISBL) investment, outside battery limits (OSBL) investment, design and engineering costs, and contingency charges. The ISBL investment is estimated based on the purchased equipment cost using the following equation [58]:

$$\mathrm{ISBL} = \sum_{i=1}^{M} C_{ei,CS}\left[(1+f_p)f_m + (f_{er}+f_{et}+f_i+f_c+f_s+f_l)\right]. \tag{16}$$

where $C_{ei,CS}$ represents the purchased equipment cost of equipment i in carbon steel material and M is the total number of pieces of equipment. The installation factors include f_p for piping, f_{er} for equipment erection, f_{et} for electrical work, f_i for instrumentation and process control, f_c for civil engineering work, f_s for structures and buildings, and f_l for lagging, insulation, or paint. The FCI is subsequently estimated using the following equation [58]:

$$\mathrm{FCI} = \mathrm{ISBL}\cdot(1+OS)\cdot(1+D\&E+X)\cdot LF, \tag{17}$$

where OS denotes the OSBL factor, $D\&E$ represents the design and engineering factor, X for the contingency charge factor and LF for the location factor. Table S.10 of the SI provides the values of the factors, categorized by the process equipment type (e.g., fluids, solids, and mixed process).

5.2. Operating expenditure

The OPEX represents the operating expenses associated with manufacturing the product [58,80,81], in this case, H_2 and solid C. OPEX is typically classified into variable and fixed production costs. Variable production costs fluctuate with plant output and include utilities and raw materials consumed during the process. In this study, variable costs include the costs for electricity, cooling water, CH_4 feed, catalyst feed, and CO_2 tax. The quantities of these inputs are determined from the mass and energy balance results of the process simulation. Baseline prices for these components are detailed in the Baseline scenario subsection.

Fixed production costs, in contrast, are independent of production levels. This study considers the following fixed costs, along with the cost estimation methods [58,81]:

1. **Operating labor costs** — operators hourly rate is assumed at $38.11 per hour per operator [82]. The plant operates in three shifts, with the required number of operators per shift, N_{OL}, estimated using [81]:

$$N_{OL} = \left(6.29 + 31.7N_{\text{solids}}^2 + 0.23N_{\text{fluids}}\right)^{0.5}, \tag{18}$$

where N_{solids} and N_{fluids} are the number of solid and fluid process equipment excluding pumps and cyclones. Operators work 49 weeks per year with 5 shifts per week.
2. **Supervision costs and laboratory charges** — estimated at 25% and 10% of operating labor costs, respectively.
3. **Direct salary overhead** — costs of providing employee benefits and training, estimated at 50% of operating labor and supervision costs.
4. **Maintenance, Taxes, insurance and operating supplies costs** — estimated at 5%, 1.5%, and 0.9% of the ISBL investment, respectively.
5. **Rent of land and environmental costs** — estimated at 1.5% and 1% of the ISBL and OSBL costs, respectively.
6. **General plant overhead** — costs of corporate overhead functions such as human resources, information technology and others, estimated at 65% of combined operating labor, supervision and direct salary overhead costs.
7. **Interest on working capital** — estimated at 9% of the working capital, which is estimated at 15% of the FCI.
8. **Patent and royalties, product distribution, and R&D costs** — estimated at 2%, 2%, and 3% of the variable and production costs, respectively.

Fixed costs are crucial even in early design stages as these costs significantly impact process economics. Some fixed costs, such as maintenance and labor, may exhibit semi-variable behavior, decreasing with increased production but persisting even at zero output [80].

5.3. Levelized cost of hydrogen

The LCOH is the cost per unit of H_2 produced over the lifetime of a H_2 production project. The LCOH is defined as the discounted cash flow divided with the discounted H_2 produced [83]:

$$\text{LCOH} = \frac{\sum_{t=1}^{t_p} \frac{\text{CAPEX}_t + \text{OPEX}_t - \text{C-Revenue}_t}{(1+i)^t}}{\sum_{t=1}^{t_p} \frac{m_{\text{H}_2,t}}{(1+i)^t}}, \tag{19}$$

where CAPEX_t represents the CAPEX in year t, OPEX_t is the OPEX in year t, and C-Revenue_t denotes the revenue of solid C in year t. $m_{\text{H}_2,t}$ is the H_2 produced in year t, while i is the fixed interest rate (discount rate). The year index, t, ranging from 1 to t_p, where t_p represents the project lifetime in years. The annual variation of CAPEX, OPEX, solid C revenue and H_2 production follows the typical start-up schedule of a chemical plant, as described by Towler and Sinnott [58], and is shown in Table S.11 of the SI.

5.4. Net present value

NPV is a useful economic measure since it allows for the time value of money and also for annual variation in expenses and revenues. The NPV of a plant is the sum of the present values of its future cash flows [58]:

$$\text{NPV} = \sum_{t=1}^{t_p} \frac{CF_t}{(1+i)^t}, \tag{20}$$

where CF_t is the cash flow of the plant in year t. The cash flow of the plant, CF_t, is calculated as:

$$CF_t = GP_t - T_t - \text{CAPEX}_t, \tag{21}$$

where GP_t and T_t is the gross profit and tax paid in year t, respectively. The gross profit, GP_t is defined as:

$$GP_t = \text{H}_2 - \text{Revenue}_t + \text{C-Revenue}_t - \text{OPEX}_t, \tag{22}$$

where $\text{H}_2 - \text{Revenue}_t$ refers to the revenue from H_2 sales in year t. The tax paid, T_t, is calculated as:

$$T_t = \begin{cases} TR \times TI_{t-1}, & \text{if } TI_{t-1} > 0 \\ 0, & \text{otherwise,} \end{cases} \tag{23}$$

where TR is the tax rate and TI_{t-1} represents the taxable income from the previous year. The taxable income in year t is given by:

$$TI_t = GP_t - Dep_t, \tag{24}$$

where Dep_t is the depreciation in year t. In this study, depreciation is assumed to follow the straight-line method over half of the project's lifetime, and inflation is considered negligible.

An attractive investment project would have a positive NPV. By calculating the NPV at different interest rate, it is possible to find the interest rate at which the NPV equals zero. This specific interest rate is known as the internal rate of return (IRR) [58].

5.5. Payback time

In this study, the PBT of the plant is defined as the fixed capital investment divided by the average annual cash flow, $\overline{CF}$ [58]:

$$\text{PBT} = \frac{\text{FCI}}{\overline{CF}}. \tag{25}$$

The average annual cash flow is based only on the years in which the plant generates revenue, i.e. year 3 onwards.

6. Results and discussions

6.1. Baseline scenario

Table 2 summarizes the parameter assumptions used for the economic evaluation of the baseline scenario. The reactor temperature in this scenario is set at 650 °C, as it provides the most cost-efficient operating conditions, as later shown in Sensitivity analyses. However, this temperature exceeds the valid range (550 °C to 600 °C) from which the catalyst kinetic and deactivation models (Eqs. (3) and (4)) were derived, making its application an extrapolation beyond the experimental basis. Reliable kinetic models for CMP that account for chemical equilibrium, reverse reactions, and adsorption are very limited in the literature, and this model was selected due to its physical relevance. To complement the baseline analysis, TEA and sensitivity analysis results at 600 °C, which also show cost-competitive performance, are provided in the SI. The average catalyst deactivation factor in the reactor is specified at 0.85. The catalyst base price is estimated using CatCost [84], based on Ni/Al_2O_3 catalyst.

The process simulation and TEA yield an estimated annual OPEX of a fully operational plant at $165 million for the CSTR model and $135 million for the PFR model. The annual OPEX is heavily influenced by variable operating costs, with CH_4 feed alone accounting for 49%–59% of the total OPEX, while fixed production costs comprise 19%–21% of the annual OPEX. Fig. 5 illustrates the breakdown of variable operating costs based on process simulations using both reactor models, while Figure S.12 of the SI presents the breakdown of fixed production costs. The main difference in the OPEX between both models stems from the catalyst feed cost. The CSTR model requires a higher catalyst feed rate of 229.21 kg h^{-1} compared to 88.93 kg h^{-1} for the PFR model to maintain an average catalyst deactivation factor of 0.85. This is mostly due to differences in the partial pressures of CH_4 and H_2 within the reactors. In the CSTR model, the partial pressures of CH_4 and H_2 remain uniform throughout the reactor at 0.48 bar and 0.64 bar, respectively. In the PFR model, partial pressures of CH_4 and H_2 vary progressively from

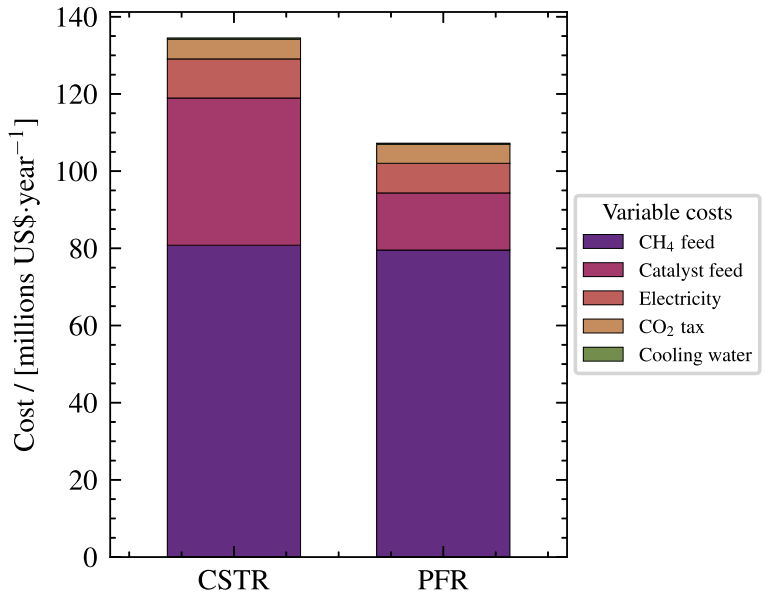

Fig. 5. Comparison of annual variable operating costs breakdown based on CMP process plant simulations using two reactor models: CSTR and PFR; highlighting the cost contributions from CH_4 feed, catalyst feed, electricity, CO_2 tax, and cooling water, with CH_4 feed costs being the most significant in both simulations.

Table 2
Baseline scenario assumptions of CMP plant and economic parameters.

Parameter	Values	Units	Remarks
Plant parameters			
Plant capacity	100	TPD	
Reactor temperature	650	°C	
Reactor pressure	1.12	bar	
Catalyst holdup	500	kg	
Catalyst bulk density	850	kg m^{-3}	Ref. [17]
Solid C bulk density	250	kg m^{-3}	Ref. [85]
Deactivation factor	0.85		
Heat source	CH_4 fuel		
PSA pressure	15	bar	
Utilization rate	0.95		
Process type	Mixed		
CO_2 capture & storage	Not applied		
Economic parameters			
Country	Netherlands		
Interest rate	0.09		
Tax rate	0.25		
Project lifetime	20	years	
CH_4 (NG) price	0.5	\$/kg	Ref. [86][a]
CO_2 tax rate	0.07151	\$/kg$_{CO_2}$	Ref. [87]
Catalyst price	20	\$/kg	Ref. [84]
Electricity price	0.1	\$/kWh	Ref. [88]
Operator's hourly rate	38.11	\$/h	Ref. [82]
H_2 price	5	\$/kg	
Solid C yearly sales	50	%	
Solid C price	1	\$/kg	
Solid C disposal	0.5	\$/kg	

[a] LHV of NG is taken as 13.1 kWh/kg.

1.0 bar and 0.12 bar at the inlet to 0.32 bar and 0.80 bar at the outlet. The partial pressures significantly influence the progression of catalyst deactivation, as described in Eq. (4).

The CSTR model results an FCI of approximately \$172 million, while the PFR model results in an FCI of approximately \$160 million. A detailed breakdown of the FCI is provided in Figure S.13 of the SI. The difference mainly comes from the direct costs of the FBR and compressors. Fig. 6 compares the breakdown of ISBL costs between the CSTR and PFR models. The higher catalyst flow rate in the CSTR model leads to a shorter catalyst residence time compared to the PFR model, resulting in less solid C holdup in the reactor. Reduced solid C holdup minimizes pressure drop, allowing for a smaller reactor design that can accommodate a reactor pressure of 1.12 bar, thus lowering reactor costs. Operating the reactor at higher pressures could potentially reduce reactor costs, as a larger pressure drop can be tolerated. However, this cannot yet be studied due to the limitations of the deactivation model employed in this study, as mentioned previously. Increasing reactor pressure should be approached cautiously, as higher pressure also reduces the equilibrium conversion of MP, as shown in Figure S.10 of the SI. The lower compressors cost for in the PFR model stems from the higher single-pass CH_4 conversion achieved by the PFR model—53.10% compared to 37.57% for the CSTR. The lower conversion in the CSTR model necessitates more recycling of the unconverted CH_4 to maintain the H_2 production at 100 TPD. As the circulating gas volume increases, the compressor workload increases, leading to higher electricity costs as reflected in Fig. 5, and necessitating larger compressors and electric motors as reflected in Fig. 6.

In this baseline scenario, it is assumed that 50% of the annual solid C production is sold for \$1.0 kg^{-1}, while the remaining 50% is disposed of at a cost of \$0.5 kg^{-1}. The resulting LCOH values are \$4.79 kg^{-1} for the CSTR model and \$3.89 kg^{-1} for the PFR model. These values fall between the LCOH for SMR, which typically ranges from \$2.25 to \$3.25 per kilogram of H_2, and for green H_2 produced via water electrolysis using renewable electricity, which has an LCOH range of \$4.90 to \$8.50 per kilogram of H_2, as reported by the IEA [89]. Assuming a H_2 selling price of \$5.0 kg^{-1}, the NPV, IRR, and PBT results for the CSTR model are 20.6 million, 6.8 years, and 0.11, respectively. For the PFR model, the results are \$186 million, 3.4 years, and 0.22, respectively. Recall that the PFR and CSTR values represent the two extremes of the expected economic performance. The specific CO_2 emissions are 3.05 kg$_{CO_2}$/kg$_{H_2}$ for the CSTR model and 2.78 kg$_{CO_2}$/kg$_{H_2}$ for the PFR model. These emissions are calculated based on the CO_2 emissions from CH_4 combustion for furnace heating and from electricity consumption, assuming CO_2 intensity of 0.286 kg$_{CO_2}$/kWh for electricity generation [90]. It is also important to mention the carbon yield of the solid C byproduct, i.e., the mass ratio between solid C and the metal catalyst, as this may determine the marketability of the solid C byproduct or the required post-processing (purification) method. The byproduct carbon yield from the CSTR model simulation is approximately 54 g_C/g_{cat}, while for the PFR model, it is 135 g_C/g_{cat}. The following section, Sensitivity analyses, assess the economic viability of the plant in alternative conditions, such as different interest rates, CH_4 prices, operator hourly rates and reactor operating parameters.

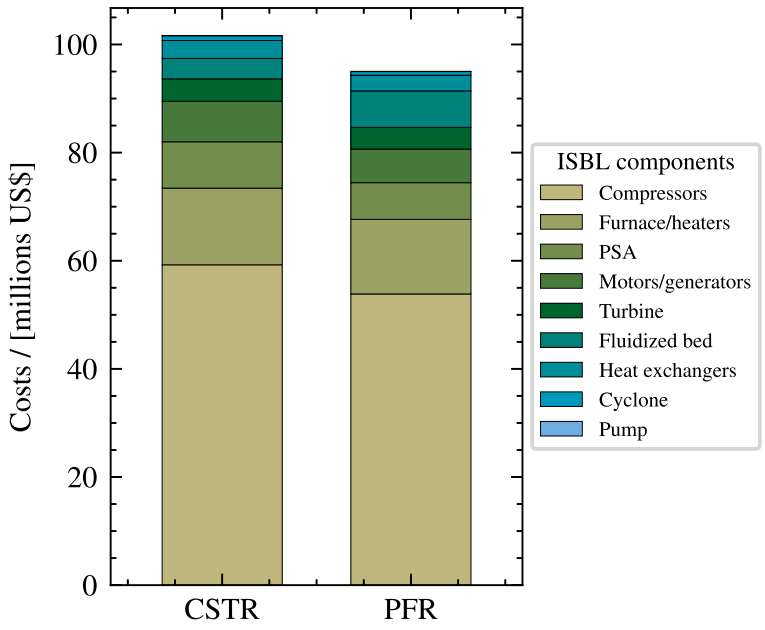

Fig. 6. Comparison of ISBL costs breakdown based on CMP process plant simulations using two reactor models: CSTR and PFR; highlighting the significance cost contribution from the compressors, furnace/heaters, PSA, motors/generators, and FBR in both systems.

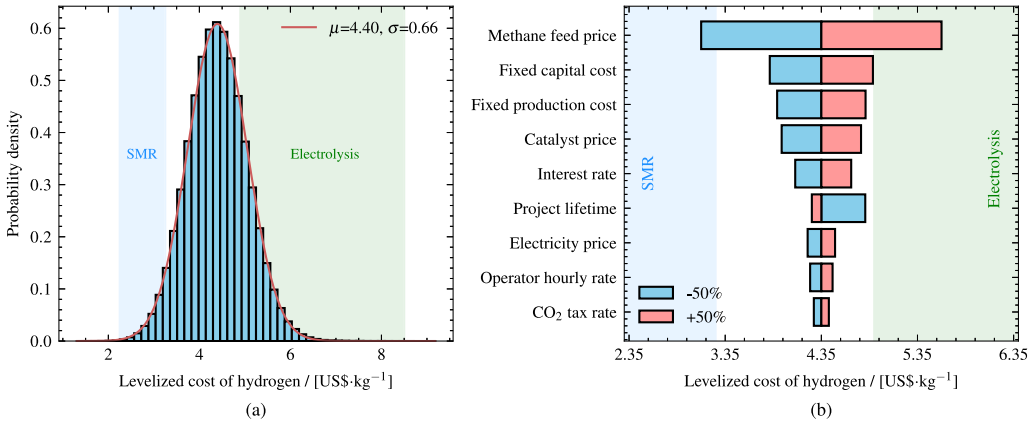

Fig. 7. Sensitivity of economic parameters on the LCOH of the CMP plant. (a) LCOH probability distribution from Monte Carlo analysis accounting for uncertainties in economic inputs, yielding a mean, μ, of \$4.39 kg^{-1} and a standard deviation, σ, of 0.66. (b) Tornado plot showing the effect of ±50% variation in each parameter on the LCOH, with CH_4 feed price being the most influential. Shaded regions in both figures represent cost benchmarks for H_2 from electrolysis via renewable energy (green) and SMR with or without CCS (blue) [89].

6.2. Sensitivity analyses

6.2.1. Economic parameters

Fig. 7a presents the probability distribution of the LCOH for the conceptual CMP, based on 1 000 000 Monte Carlo samples [91]. The LCOH values presented are based on the TEA of a plant operating with conditions averaged between the CSTR and PFR model simulations. The histogram illustrates the distribution of LCOH outcomes resulting from uncertainties in key economic input parameters, including the fixed capital cost (ISBL estimation), fixed production cost, interest rate, project lifetime, CH_4 feed price, electricity price, catalyst price, operator hourly rate, and CO_2 tax rate. The overlaid red curve represents the probability density function of the fitted distribution. Additional details on the Monte Carlo sensitivity analysis are provided in the SI. The analysis results in a mean LCOH of \$4.39 kg^{-1}, with a standard deviation of 0.66. These findings suggest that the CMP process is likely to be more cost-competitive than electrolysis via renewable energy given the considered economic uncertainties.

Fig. 7b presents a sensitivity analysis of each of the economic parameters on the LCOH. The base LCOH for CMP plant operating with conditions averaged between the two reactor simulations is \$4.34 kg^{-1}. The analysis identifies the CH_4 feed price as the most critical factor influencing LCOH, thus play a pivotal role in determining the economic viability of CMP for large-scale H_2 production. The ±50% variation in the CH_4 price reflects the expected differences in LCOH when the plant is constructed in different regions worldwide. Fixed capital cost, fixed production costs and catalyst price exert moderate influence. The capital cost estimates in this study have an uncertainty of ±30% due to limited cost data and design details. This leads to approximately 6%variation in LCOH, suggesting the estimates are adequate for the TEA of CMP plants. Fixed production costs are partially estimated based on operating labor expenses, highlighting the importance of incorporating up-to-date assumptions for operator rates to ensure realistic TEA results that reflect latest labor market conditions. Catalyst price is another influential factor, underscoring the importance of catalyst recovery, which will be discussed in a future study.

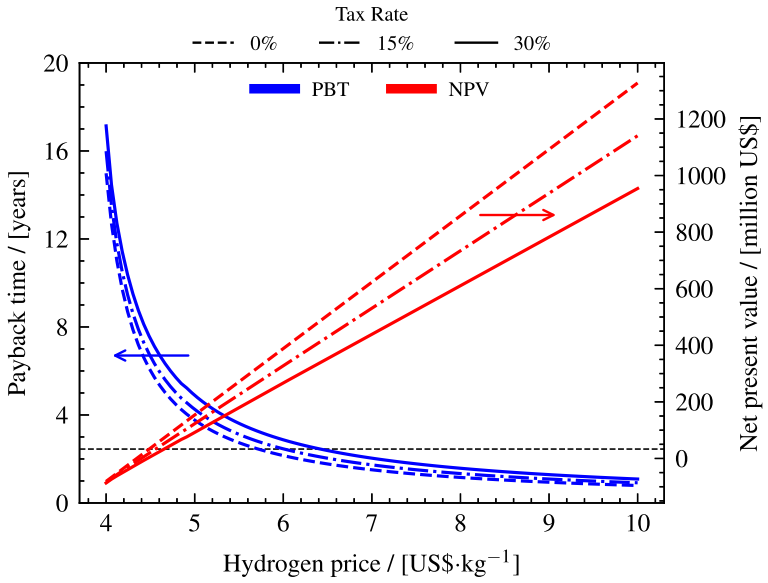

Fig. 8. Relationship between H_2 price, PBT, and NPV of the CMP plant at varying tax rates (0%, 15%, and 30%). As H_2 price increases, PBT decreases, and NPV rises. Higher taxes slightly reduce profitability of the plant.

Fig. 8 illustrates the relationship between the selling price of H_2 and the financial feasibility of a CMP plant, as measured by PBT and NPV at varying tax rates (0%, 15%, and 30%). As H_2 selling price increases from \$0 to \$10 per kilogram, the PBT decreases, indicating a faster investment recovery, while the NPV rises, indicating greater profitability. At an H_2 price of approximately \$5.0 kg^{-1}, the PBT is approximately 5 years, with an NPV of around \$100 million, suggesting economic feasibility. Higher H_2 selling prices further improve the profitability of the plant, with a PBT of approximately one year and an NPV exceeding \$1 billion at \$10 kg^{-1}. Higher tax rates reduce profitability, particularly at high H_2 prices. This plot highlights the dependency of project feasibility on H_2 market prices and tax policies. Figure S.14 of the SI presents the NPV as a function of interest rate and project lifetime, showing that the IRR values for project lifetimes of 10, 20, and 30 years, respectively.

6.2.2. Solid carbon sales and disposal

Fig. 9 illustrates the LCOH as a function of solid C price, annual sales percentage, and disposal fees, providing insights into how revenue from solid C sales and associated disposal costs influence the economic feasibility of CMP. As the solid C price increases, the LCOH decreases because the revenue generated offsets H_2 production costs. This effect is more pronounced when a larger percentage of the annual solid C production is sold. The three panels in the figure show different fee values for disposing the unsold solid C byproduct. As the fees increase from \$0 to \$2 per kilogram, the LCOH rises, reflecting the additional cost burden of sequestering solid C.

In this study, H_2 is considered the primary product of the plant, while solid C is treated as a byproduct. Fig. 9 indicates that the CMP process can achieve LCOH values within or below the SMR range at relatively low solid C prices—well below the typical price range for CNTs or CNFs, which can be synthesized using Ni-based catalysts. The results also show that CMP would not be competitive with SMR if focused solely for H_2 production without selling the solid C byproduct, even in scenarios with zero disposal fees. The NPV plot as a function of solid C sales and fees, shown in Figure S.15 of the SI, indicates that achieving a positive NPV requires some revenue from the sales of the solid C byproduct. Moreover, the solid C can also have environmental consequences if not sequestered properly. Alternatively, CMP plants can also be built for the production of advanced nanocarbons as it main purpose, such as CNTs and CNFs, with the H_2 taken as a fuel for the process or a byproduct sold at minimal cost. This type of CMP plant would likely operate on a smaller scale, given that the global demand for nanocarbons is significantly lower than that for H_2 fuels. This plant may also required a purification step to remove catalyst residues from the nanocarbon products. As mentioned previously, the separation of catalyst and carbon remains an important yet unresolved challenge. In our ongoing work, we are exploring potential separation methods, supported by both experimental studies and process modeling.

6.2.3. Reactor temperature

Fig. 10a to d presents the LCOH, reactor single-pass CH_4 conversion, catalyst mass flow rate, and flow rate of the recycled CH_4 as functions of the reactor temperature, based on the CMP process plant simulations using the CSTR and PFR models. The simulations were conducted at reactor temperatures ranging from 550 °C to 700 °C in increments of 25 °C. In both models, the LCOH reaches a minimum at 650 °C, as shown in Fig. 10a, with values of \$4.79 kg^{-1} for the CSTR and \$3.89 kg^{-1} for the PFR, resulting in an average minimum LCOH of \$4.34 kg^{-1}. At temperatures below 650 °C, both reactor models show an increase in LCOH. This increase can be attributed to the lower single-pass CH_4 conversion rates at reduced temperatures, as shown in Fig. 10b, which necessitate higher capital and operating costs to meet H_2 production capacity of 100 TPD. Both CH_4 conversion and conversion efficiency improve with increasing temperature. Figure S.16 of the SI shows the conversion efficiency as a function of temperature. However, above 650 °C, the LCOH increases again for both reactor models, particularly for the CSTR. This is primarily due to the significantly increased catalyst flow rates required to maintain catalyst activity inside the reactor at elevated temperatures, as shown in Fig. 10c, leading to higher catalyst costs. Note that the deactivation of the catalysts is caused by the encapsulation of active catalytic sites with solid C product. As reaction rates increase with temperature, following the Arrhenius equation, the formation of solid C accelerates and deactivation is more pronounced, necessitating faster catalyst replenishment thus increasing the OPEX.

Recall that the CSTR and PFR models represent the two extremes of FBR operating conditions. Consequently, the performance of an actual fluidized bed CMP reactor – such as LCOH, CH_4 conversion, and catalyst rate – is expected to fall between the values calculated for these two models. If mixing is more pronounced, the performance of the reactor will approach the CSTR values, whereas reduced mixing will

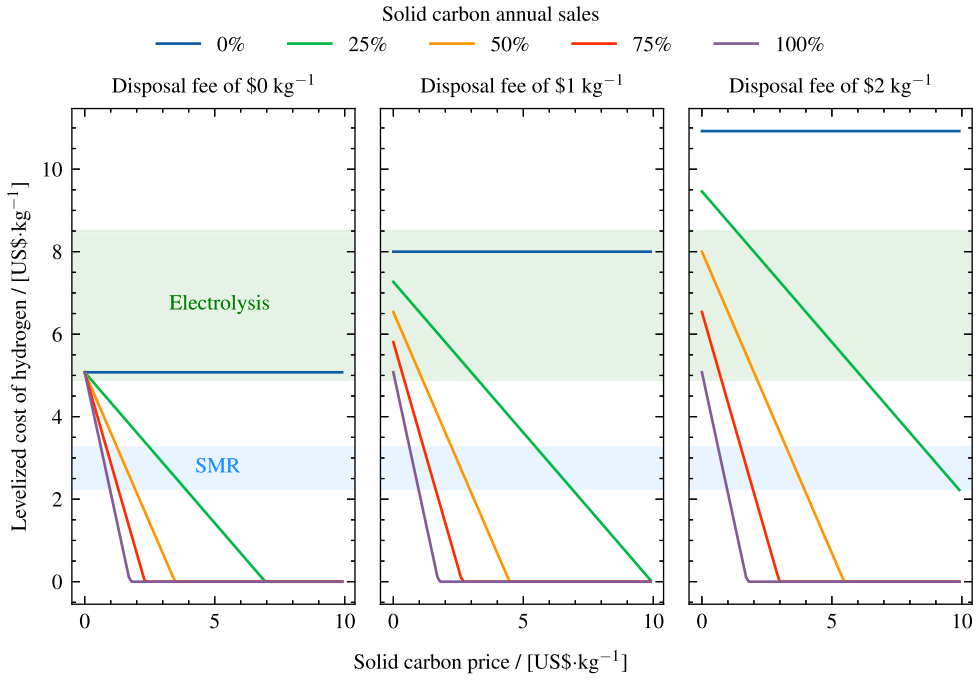

Fig. 9. LCOH as a function of solid C price (in $/kg), at varying assumptions of solid C annual sales percentages and solid C disposal (sequestration) fees. The three panels represent different disposal fee scenarios, with the left panel showing a fee of $\$0\,kg^{-1}$, the middle panel $\$1\,kg^{-1}$, and the right panel $\$2\,kg^{-1}$. The cost ranges for H_2 production via electrolysis and SMR are highlighted for comparison [89].

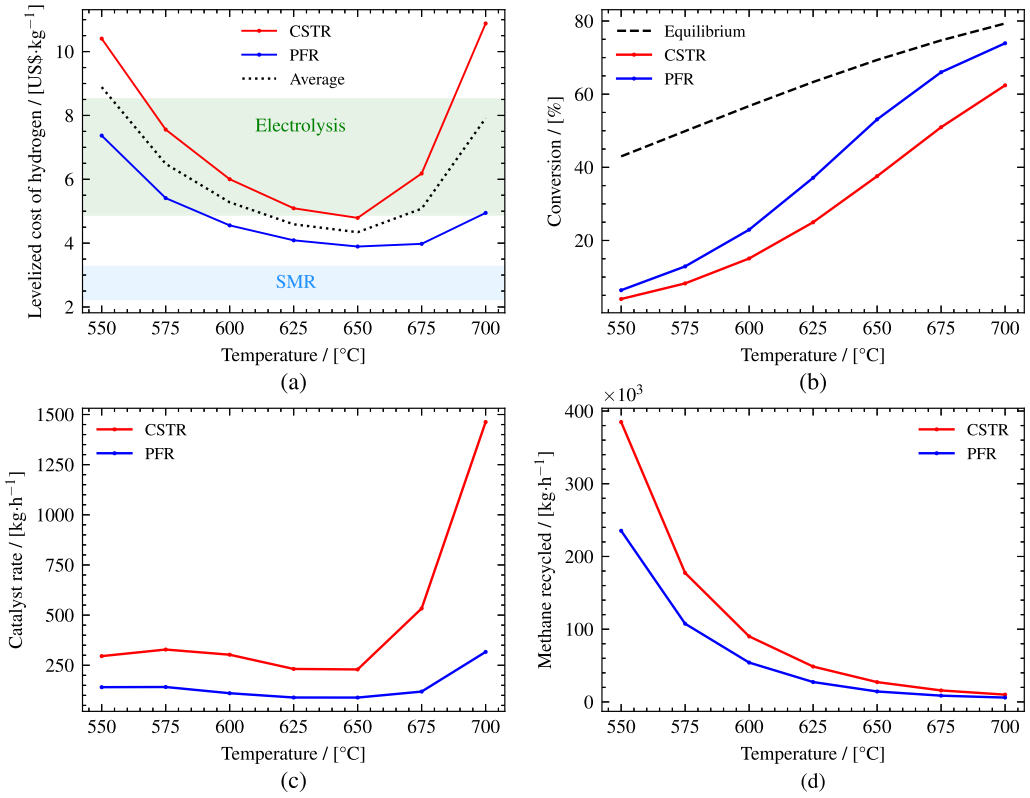

Fig. 10. Comparison between CSTR and PFR models for CMP process plant simulations, showing (a) LCOH, (b) reactor CH_4 conversion, (c) catalyst flow rate, and (d) CH_4 recycle flow rate as functions of reactor temperature. At lower temperatures, the LCOH is relatively high due to low reaction conversion, which reduces H_2 production efficiency due to increased CH_4 recycling. At higher temperatures, the LCOH increases again due to the significant rise in catalyst costs. The lowest production costs are found within 625 °C to 675 °C.

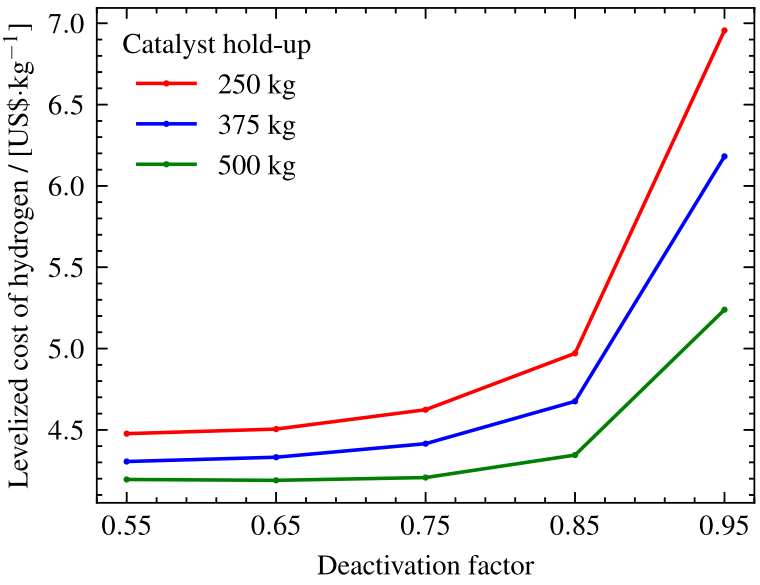

Fig. 11. LCOH as a function of catalyst deactivation factor and catalyst holdup inside the reactor. While higher CH_4 conversion is achieved at a higher deactivation factor, the resulting increase in catalyst feed cost generally offsets this benefit. However, at a catalyst holdup of 500 kg, the minimum LCOH occurs at a deactivation factor of 0.65. Beyond a deactivation factor of 0.85, the LCOH increases due to a significant rise in catalyst feed costs.

result in values closer to those of the PFR. The temperature sensitivity results for LCOH shows that the difference in LCOH between CSTR and PFR varies with temperature. At lower temperatures, the relatively small difference in CH_4 conversion between the two models leads to a notable discrepancy in the amount of CH_4 recycled within the plant, as shown in Fig. 10d, thereby resulting in a similar discrepancy in production costs. Above 650 °C, the calculated catalyst requirements for the two models diverge more significantly due to accelerated catalyst deactivation rates, leading to large differences in the predicted LCOH values between the CSTR and PFR.

The analysis shows that reaction temperature is a critical reactor parameter that significantly influence the economic feasibility of CMP. Operating at the optimal temperature can minimize production costs, making CMP competitive with green H_2 production. However, without additional revenue from solid C sales, the cost of H_2 from CMP remains significantly higher than conventional SMR, with LCOH ranging from $2.25 to $3.25 per kilogram [89]. From the discussion, it can be inferred that the profile of the LCOH-temperature curve is highly sensitive to electricity and catalyst prices. Figures S.17a and S.17b in the SI illustrate LCOH as a function of reactor temperature for varying electricity and catalyst prices.

6.2.4. Catalyst holdup and average deactivation factor

Fig. 11 illustrates the LCOH results as a function of the catalyst deactivation factor and the catalyst holdup within the reactor. The LCOHs shown are derived from the TEA of the CMP plant operating with conditions averaged between the CSTR and PFR model simulations. The deactivation factor, ranging from 0.55 to 0.95, represents the extent of average catalyst deactivation inside the reactor. The three curves correspond to different catalyst holdup scenarios, highlighting how the amount of catalyst in the reactor impacts production costs at various levels of catalyst deactivation. As the deactivation factor increases, catalyst activity improves, leading to higher CH_4 conversion thereby enhancing plant efficiency. However, maintaining a high deactivation factor requires a higher catalyst flow rate into and out of the reactor, which increases production costs. Figure S.18 of the SI shows the catalyst flow rate as a function of catalyst holdup and deactivation factor in the reactor. The conversion gains from a higher deactivation factor are almost always offset by the cost of the catalyst feed, except in the case of a 500 kg catalyst holdup, where the minimum LCOH is reached at a deactivation factor of 0.65. Beyond a deactivation factor of 0.85, the LCOH rises sharply across all holdup scenarios.

An increase in catalyst holdup substantially reduces the LCOH. A higher catalyst amount provides more active sites for the reaction, enabling higher single-pass conversion rates of CH_4. This reduces the amount of unconverted CH_4 that needs to be recycled, thereby decreasing overall energy and processing costs. This improvement offsets the additional capital costs associated with a larger reactor volume required to accommodate the increased holdup. The sensitivity analyses were conducted with catalyst holdup values up to 500 kg. For catalyst holdup exceeding 500 kg, the CSTR simulations failed to converge. This occurs because the large catalyst holdup leads to elevated H_2 concentrations in the reactor. In this condition, backward MP reaction becomes more profound, preventing any observable catalyst deactivation and hindering numerical convergence.

6.2.5. Plant capacity

Fig. 12 presents the LCOH results for CMP plant operating with conditions averaged between the two reactor simulations across a range of capacities from 12.5 to 800 TPD. The chart provides the breakdown of the LCOH, highlighting the contributions from various levelized cost components (i.e., the discounted costs per kilogram of discounted H_2 produced), including utilities, raw materials, CO_2 tax, CAPEX, fixed production costs, and revenue from solid C sales. The LCOH decreases significantly as plant capacity increases, particularly in the range from 12.5 to 200 TPD. This trend highlights the presence of economies of scale, where larger production capacities lead to lower specific costs. Beyond 200 TPD, the reduction in LCOH continues, albeit at a much slower pace, suggesting that the most substantial cost benefits are realized at lower to mid-range capacities.

The primary drivers of cost improvement with increasing plant capacity are the reductions in levelized fixed production costs and CAPEX. In this study, the fixed production costs are estimated based on plant operating labor and capital costs. Labor costs are highly dependent on the number of operators hired, which is estimated using Eq. (18). Since the total number of process equipment varies only slightly across plant capacities – only the size of the equipment changing significantly – there is a notable improvement in fixed production costs per kilogram of H_2 as the capacity increases. In practice, the labor costs for smaller plants (≤25 TPD) could potentially be reduced by assigning operators to

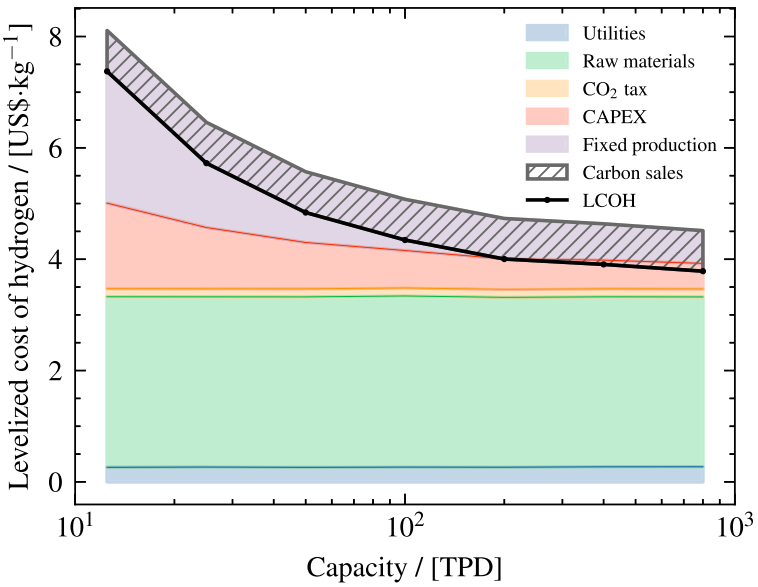

Fig. 12. LCOH for CMP plants across capacities (12.5 to 800 TPD) are shown. The stacked line chart breaks down LCOH, highlighting contributions from various cost factors. The overall trend shows a significant reduction in LCOH with increasing plant capacity, particularly from 12.5 TPD to 200 TPD, mainly driven by reduced levelized fixed production costs and CAPEX per kilogram of H_2 produced.

manage multiple components. However, this prediction would require a more detailed plant engineering design to validate. The reduction in levelized CAPEX reflects the economies of scale associated with the cost of the plant itself. In the existing literature, CAPEX estimation models for any type of CMP plants are scarce. This study uses the FCI estimations for CMP plants across various capacities to develop a capital cost curve, formulated as follows:

$$C = \frac{C_0}{S_0^n} \times S^n = mS^n, \tag{26}$$

where C is the FCI of the plant, S is the plant capacity, m is the cost curve constant, and n is the cost exponent. By fitting the average FCI results from CMP plant simulations using CSTR and PFR reactor models to this equation, the cost curve constant, m, is determined to be \$3.73 million and the cost exponent, n, is found to be 0.821. The curve is illustrated in Figure S.19 of the SI. This cost curve is suitable for making order-of-magnitude ("Class 5") estimates of CMP plant costs [58].

The costs associated with utilities, raw materials, and CO_2 tax remain relatively constant across the range of plant capacities. This stability can be attributed to the nature of these costs. Utilities, such as electricity and cooling water, scale directly with the gas flows in the plant, which are proportional to H_2 production. Similarly, raw materials, primarily the CH_4 feedstock, scale directly with output, resulting in a consistent cost per kilogram of H_2. The CO_2 tax is also linear, as the amount of fuel combusted for reactor heating increases with capacity. To reduced these costs, the overall efficiency of the plant needs to be improved. This can be achieved by improving equipment efficiency, optimizing heat integration, and minimizing entropy production.

6.3. Heating methods and CCS

Fig. 13 presents the LCOH and specific CO_2 emissions from a CMP plant operating with conditions averaged between the CSTR and PFR model simulations in different reactor heating scenarios. The reactor heating methods considered include CH_4 combustion with and without CCS, H_2 combustion, and electric heating powered by grid electricity. The efficiency of the furnace is 0.85 for fuel combustion and 0.90 for electric heating. The capital and operating costs for carbon capture are estimated based on the IEA 2023 CCUS report, which provides a levelized cost of CO_2 capture of approximately \$0.085/kg_{CO_2} [92]. The analysis shows that the specific CO_2 emissions from CMP are lower than those from SMR (10.1–17.2 kg CO_2/kg H_2) and comparable to those from renewable-powered water electrolysis (0.5–2.5 $kgCO_2/kgH_2$) [93].

Across all scenarios, H_2 combustion yields the highest LCOH and the second lowest CO_2 emissions. The increased cost is primarily attributed to the higher CH_4 feed and recycling requirement, to produce H_2 fuel for heating, in addition to the 100 TPD of H_2 required for plant production. This has cost implication on both OPEX and CAPEX. Furthermore, the increased gas circulation within the plant necessitates higher power consumption for compressors. As the electricity required to operate these compressors is assumed to be sourced from the grid, with a CO_2 intensity of 0.286 kg_{CO_2}/kWh [90], this further contributes to the overall CO_2 emissions of the plant. Electric heating also results in high CO_2 emissions if the electricity source is coming from the same grid. For electric heating to be more environmentally sustainable than alternative heating methods, it would need to be entirely powered by renewable energy sources. Additionally, the purchase cost of electric heaters is higher compared to fired heaters, which significantly increases the overall levelized cost of the plant. Heating with CH_4 combustion, both with and without CCS, incurs similar costs, as the capital and operating costs associated with CCS are nearly equivalent to the carbon tax that would be paid in the absence of CCS. The analysis shows that only heating with CH_4 combustion results in a positive NPV with a H_2 selling price of \$5 kg^{-1}. In conclusion, the most cost-effective and low-emission solution would be to utilize CH_4 combustion with CCS for heating the reactor.

Conclusions and recommendations

This study presents an economic assessment of CMP with Ni-based catalyst in FBR, highlighting its potential as a sustainable H_2 production technology. The developed plant modeling framework integrates reactor modeling and plant-scale simulations, capturing the interplay between reaction kinetics and catalyst deactivation. Using two reactor models, based on ideal CSTR and PFR, this work captured the operational extremes of CMP in fluidized beds and predicted of the corresponding economic limits. CMP offers a competitive pathway for H_2 production, with an LCOH ranging from \$3.89 to \$4.79 per kilogram in the baseline scenario. Monte Carlo sensitivity analysis, capturing uncertainties in economic parameters, yields a mean LCOH of \$4.39 kg^{-1}

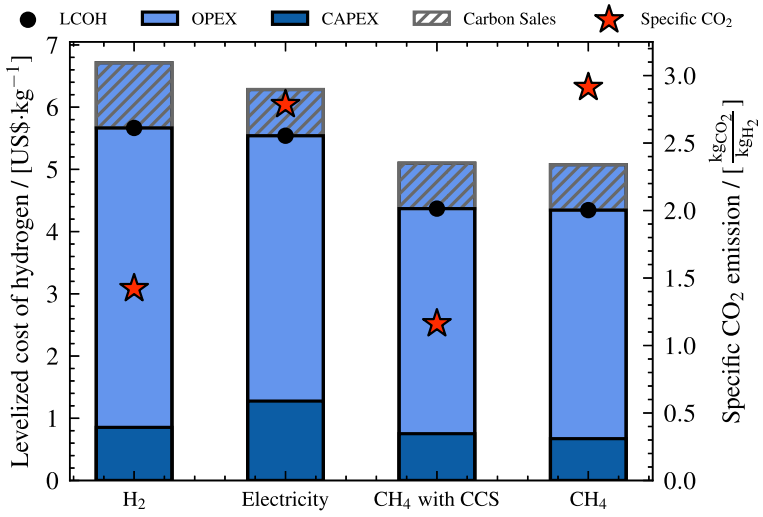

Fig. 13. LCOHs and specific CO_2 emissions from CMP plant process simulation in different reactor heating scenarios are presented. The LCOH is broken down into levelized CAPEX and OPEX, with cost offsets from carbon sales. The specific CO_2 emissions are plotted on the secondary *y*-axis. The heating methods analyzed include CH_4 combustion with and without CCS, H_2 combustion, and electric heating. H_2 combustion leads to the highest LCOH, while CH_4 combustion results in the highest CO_2 emissions. Integrating CCS into CH_4 combustion significantly reduces emissions while maintaining a relatively low overall cost.

with a standard deviation of 0.66. While generally more expensive than SMR, CMP has lower emissions and remains a lower-cost alternative to water electrolysis using renewable energy. Reactor performance, particularly CH_4 conversion and catalyst deactivation, significantly influences economic outcomes. The minimum LCOH is achieved at a reactor temperature of 650 °C, which balance the reactor conversion and catalyst costs. The plant capacity sensitivity analysis shows substantial cost reductions as capacity increases. Revenue from the solid C byproduct could offset H_2 production costs, potentially making CMP economically superior to SMR. If solid C cannot be sold, sequestration costs may challenge the feasibility of CMP. Further research should focus on developing CMP catalysts with improved resistance to high-temperature deactivation can enable higher conversion rates with lower catalyst requirements. The catalyst should also be developed with an emphasis on cost-effectiveness, as its price plays a crucial role in the economic feasibility of CMP. Expanding kinetic and deactivation experiments across a broader range of temperatures and pressures will lead to more robust models and more reliable economic predictions. As mentioned previously, the models in this study were extended beyond the validated temperature range in the simulations. This may have introduced inaccuracies, as CMP can exhibit different mechanisms and kinetics across temperature regimes [94]. Experiments should also be carried out using industrial CH_4 feedstocks to capture the influence of contaminants and other hydrocarbons on reaction and catalyst deactivation. Future studies should also prioritize carbon–catalyst separation to enable solid carbon purification and valorization, alongside catalyst recycling and regeneration. This should involve a comprehensive life-cycle assessment and solid C market analysis to evaluate the overall sustainability of the process and ensure that the carbon product meets commercial specifications. This would allow assessment of the potential of CMP for producing advanced nanocarbons as primary products in place of H_2.

CRediT authorship contribution statement

P.B. Tamarona: Writing – original draft, Software, Methodology, Investigation, Formal analysis, Conceptualization. **T.M.J. Nijssen:** Writing – review & editing, Validation. **T.J.H. Vlugt:** Writing – review & editing, Supervision, Resources, Project administration, Funding acquisition. **M. Ramdin:** Writing – review & editing, Supervision.

Declaration of competing interest

The authors declare the following financial interests/personal relationships which may be considered as potential competing interests: Thijs J.H. Vlugt reports financial support was provided by Advanced Research Center for Chemical Building Blocks. If there are other authors, they declare that they have no known competing financial interests or personal relationships that could have appeared to influence the work reported in this paper.

Acknowledgments

This work is part of the Advanced Research Center for Chemical Building Blocks, ARC CBBC, which is co-founded and co-financed by the Dutch Research Council (NWO), Netherlands and the Netherlands Ministry of Economic Affairs and Climate Policy.

Appendix A. Supplementary data

The supporting information provides the details of the process simulation workflow, process flow diagrams with stream information, techno-economic and sensitivity analyses for simulations at 600 °C, and details of the Monte Carlo sensitivity analysis. Supporting tables include the list of equipment cost correlations, FCI factors, and the adapted plant start-up schedule used in this study. Supporting figures include plots of MP equilibrium conversion, PSA pressure sensitivity, breakdowns of fixed production costs and FCI, NPV sensitivity analyses, conversion efficiency as a function of reactor temperature, LCOH at varying electricity and catalyst prices, catalyst flow rate as a function of catalyst holdup and deactivation, and the capital cost curve.

Supplementary material related to this article can be found online at https://doi.org/10.1016/j.cej.2025.167134.

Data availability

The processing codes and process simulations developed in this work can be found in the following GitHub repository: https://github.com/pbtamarona/methanepyrolysis.

References

[1] IPCC Climate Change 2023: Synthesis Report. Contribution of Working Groups I, II and III To the Sixth Assessment Report of the Intergovernmental Panel on Climate Change [Core Writing Team, H. Lee and J. Romero (Eds.)], First ed., 2023, pp. 35–115.

[2] S.V. Feigin, D.O. Wiebers, G. Lueddeke, S. Morand, K. Lee, A. Knight, M. Brainin, V.L. Feigin, A. Whitfort, J. Marcum, T.K. Shackelford, L.F. Skerratt, A.S. Winkler, Proposed solutions to anthropogenic climate change: A systematic literature review and a new way forward, Heliyon 9 (2023) e20544.

[3] IEA global hydrogen review 2024, 2024.

[4] M.R.G. Pangestu, Z. Malaibari, A. Muhammad, F.N. Al-Rowaili, U. Zahid, Comprehensive review on methane pyrolysis for sustainable hydrogen production, Energy Fuels 38 (2024) 13514–13538.

[5] M. Shokrollahi, N. Teymouri, O. Ashrafi, P. Navarri, Y. Khojasteh-Salkuyeh, Methane pyrolysis as a potential game changer for hydrogen economy: Techno-economic assessment and GHG emissions, Int. J. Hydrog. Energy 66 (2024) 337–353.

[6] N. Sánchez-Bastardo, R. Schlögl, H. Ruland, Methane pyrolysis for zero-emission hydrogen production: A potential bridge technology from fossil fuels to a renewable and sustainable hydrogen economy, Ind. Eng. Chem. Res. 60 (2021) 11855–11881.

[7] J. Song, S. Park, Review of methane pyrolysis for clean turquoise hydrogen production, J. Anal. Appl. Pyrolysis 183 (2024) 106727.

[8] Y.H. Chan, Z.P. Chan, S.S.M. Lock, C.L. Yiin, S.Y. Foong, M.K. Wong, M.A. Ishak, V.C. Quek, S. Ge, S.S. Lam, Thermal pyrolysis conversion of methane to hydrogen (H2): A review on process parameters, reaction kinetics and techno-economic analysis, Chin. Chem. Lett. 35 (2024) 109329.

[9] T. Becker, M. Richter, D.W. Agar, Methane pyrolysis: Kinetic studies and mechanical removal of carbon deposits in reactors of different materials, Int. J. Hydrog. Energy 48 (2023) 2112–2129.

[10] I. Durán, B. Dietrich, C. Hofberger, L. Stoppel, N. Uhlenbruck, T. Wetzel, CO2 impact on methane pyrolysis as a key issue of using biogas as an educt: A theoretical study, Int. J. Energy Res. 2023 (2023) 3684046, _eprint: https://onlinelibrary.wiley.com/doi/pdf/10.1155/2023/3684046.

[11] S.R. Patlolla, K. Katsu, A. Sharafian, K. Wei, O.E. Herrera, W. Mérida, A review of methane pyrolysis technologies for hydrogen production, Renew. Sustain. Energy Rev. 181 (2023) 113323.

[12] J. Prabowo, L. Lai, B. Chivers, D. Burke, A.H. Dinh, L. Ye, Y. Wang, Y. Wang, L. Wei, Y. Chen, Solid carbon co-products from hydrogen production by methane pyrolysis: Current understandings and recent progress, Carbon 216 (2024) 118507.

[13] T. Keipi, K.E.S. Tolvanen, H. Tolvanen, J. Konttinen, Thermo-catalytic decomposition of methane: The effect of reaction parameters on process design and the utilization possibilities of the produced carbon, Energy Convers. Manage. 126 (2016) 923–934.

[14] J. Riley, C. Atallah, R. Siriwardane, R. Stevens, Technoeconomic analysis for hydrogen and carbon Co-Production via catalytic pyrolysis of methane, Int. J. Hydrog. Energy 46 (2021) 20338–20358.

[15] K. Bae, D. Kim, P.A. Dung, D. Lee, B. Hwang, K.S. Go, W. Kim, J.K. Lee, J.S. Im, S.C. Kang, S.H. Lee, Simultaneous and continuous production of carbon nanotubes and hydrogen by catalytic CH4 decomposition in a pressurized Fluidized-Bed reactor, Ind. Eng. Chem. Res. 63 (2024) 930–941.

[16] S. Pathak, E. McFarland, Iron catalyzed methane pyrolysis in a stratified fluidized bed reactor, Energy Fuels 38 (2024) 12576–12585.

[17] M. Hadian, D.P.F. Marrevee, K.A. Buist, B.H. Reesink, A.N.R. Bos, A.P. Bavel, J.A.M. Kuipers, Kinetic study of thermocatalytic decomposition of methane over nickel supported catalyst in a fluidized bed reactor, Chem. Eng. Sci. 260 (2022) 117938.

[18] K.R. Parmar, K.K. Pant, S. Roy, Blue hydrogen and carbon nanotube production via direct catalytic decomposition of methane in fluidized bed reactor: Capture and extraction of carbon in the form of CNTs, Energy Convers. Manage. 232 (2021) 113893.

[19] M. Dadsetan, M.F. Khan, M. Salakhi, E.R. Bobicki, M.J. Thomson, CO2-free hydrogen production via microwave-driven methane pyrolysis, Int. J. Hydrog. Energy 48 (2023) 14565–14576.

[20] R. Siriwardane, J. Riley, C. Atallah, M. Bobek, Investigation of methane and ethane pyrolysis with highly active and durable iron-alumina catalyst to produce hydrogen and valuable nano carbons: Continuous fluidized bed tests and reaction rate analysis, Int. J. Hydrog. Energy 48 (2023) 14210–14225.

[21] M. Hadian, J.G. Ramírez, M.J.A. de Munck, K.A. Buist, A.N.R. Bos, J.A.M. Kuipers, Comparative analysis of a batch and continuous fluidized bed reactors for thermocatalytic decomposition of methane: A CFD-DEM-MGM approach, Chem. Eng. J. 484 (2024) 149478.

[22] E. Sun, et al., A semi-continuous process for co-production of CO2-free hydrogen and carbon nanotubes via methane pyrolysis, Cell Rep. Phys. Sci. 4 (2023) 101338.

[23] N. Shah, S. Ma, Y. Wang, G.P. Huffman, Semi-continuous hydrogen production from catalytic methane decomposition using a fluidized-bed reactor, Int. J. Hydrog. Energy 32 (2007) 3315–3319.

[24] X. Zhang, A. Kätelhön, G. Sorda, M. Helmin, M. Rose, A. Bardow, R. Madlener, R. Palkovits, A. Mitsos, CO2 mitigation costs of catalytic methane decomposition, Energy 151 (2018) 826–838.

[25] B.J. Leal Pérez, J.A. Medrano Jiménez, R. Bhardwaj, E. Goetheer, M. van Sint Annaland, F. Gallucci, Methane pyrolysis in a molten gallium bubble column reactor for sustainable hydrogen production: Proof of concept & techno-economic assessment, Int. J. Hydrog. Energy 46 (2021) 4917–4935.

[26] F. Pruvost, S. Cloete, J. Hendrik Cloete, C. Dhoke, A. Zaabout, Techno-Economic assessment of natural gas pyrolysis in molten salts, Energy Convers. Manage. 253 (2022) 115187.

[27] F. Angikath, F. Abdulrahman, A. Yousry, R. Das, S. Saxena, O. Behar, H. Alhamed, T. Altmann, B. Dally, S.M. Sarathy, Technoeconomic assessment of hydrogen production from natural gas pyrolysis in molten bubble column reactors, Int. J. Hydrog. Energy 49 (2024) 246–262.

[28] B. Parkinson, M. Tabatabaei, D.C. Upham, B. Ballinger, C. Greig, S. Smart, E. McFarland, Hydrogen production using methane: Techno-economics of decarbonizing fuels and chemicals, Int. J. Hydrog. Energy 43 (2018) 2540–2555.

[29] G.A.V. Wald, M.S. Masnadi, D.C. Upham, A.R. Brandt, Optimization-based techno-economic analysis of molten-media methane pyrolysis for reducing industrial sector CO2 emissions, Sustain. Energy Fuels 4 (2020) 4598–4613.

[30] Palo Emma, Cosentino Vittoria, Iaquaniello Gaetano, Thermal methane cracking on molten metal: Techno-economic assessment, Chem. Eng. Trans. 105 (2023) 97–102.

[31] J. Zhang, X. Li, H. Chen, M. Qi, G. Zhang, H. Hu, X. Ma, Hydrogen production by catalytic methane decomposition: Carbon materials as catalysts or catalyst supports, Int. J. Hydrog. Energy 42 (2017) 19755–19775.

[32] N. Muradov, Hydrogen via methane decomposition: an application for decarbonization of fossil fuels, Int. J. Hydrog. Energy 26 (2001) 1165–1175.

[33] R. Kundu, V. Ramasubramanian, S.T. Neeli, H. Ramsurn, Catalytic pyrolysis of methane to hydrogen over carbon (from cellulose biochar) encapsulated iron nanoparticles, Energy Fuels 35 (2021) 13523–13533.

[34] V. Shilapuram, N. Ozalp, M. Oschatz, L. Borchardt, S. Kaskel, R. Lachance, Thermogravimetric analysis of activated carbons, ordered mesoporous carbide-derived carbons, and their deactivation kinetics of catalytic methane decomposition, Ind. Eng. Chem. Res. 53 (2014) 1741–1753.

[35] P. Lott, M.B. Mokashi, H. Müller, D.J. Heitlinger, S. Lichtenberg, A.B. Shirsath, C. Janzer, S. Tischer, L. Maier, O. Deutschmann, Hydrogen production and carbon capture by gas-phase methane pyrolysis: A feasibility study, ChemSusChem 16 (2023) e202201720.

[36] L. Fulcheri, V.-J. Rohani, E. Wyse, N. Hardman, E. Dames, An energy-efficient plasma methane pyrolysis process for high yields of carbon black and hydrogen, Int. J. Hydrog. Energy 48 (2023) 2920–2928.

[37] R.B. Raja, R. Sarathi, R. Vinu, Selective production of hydrogen and solid carbon via methane pyrolysis using a swirl-induced point–plane non-thermal plasma reactor, Energy Fuels 36 (2022) 826–836.

[38] M. Abuseada, C. Wei, R.M. Spearrin, T.S. Fisher, Solar–Thermal production of graphitic carbon and hydrogen via methane decomposition, Energy Fuels 36 (2022) 3920–3928.

[39] R.A. Dagle, V. Dagle, M.D. Bearden, J.D. Holladay, T.R. Krause, S. Ahmed, An overview of natural gas conversion technologies for co-production of hydrogen and value-added solid carbon products, 2017.

[40] E. Tezel, H.E. Figen, S.Z. Baykara, Hydrogen production by methane decomposition using bimetallic Ni–Fe catalysts, Int. J. Hydrog. Energy 44 (2019) 9930–9940.

[41] A.S. Al-Fatesh, A.H. Fakeeha, A.A. Ibrahim, W.U. Khan, H. Atia, R. Eckelt, K. Seshan, B. Chowdhury, Decomposition of methane over alumina supported Fe and Ni–Fe bimetallic catalyst: Effect of preparation procedure and calcination temperature, J. Saudi Chem. Soc. 22 (2018) 239–247.

[42] S.H. Sharif Zein, A.R. Mohamed, P.S. Talpa Sai, Kinetic studies on catalytic decomposition of methane to hydrogen and carbon over Ni/TiO2 catalyst, Ind. Eng. Chem. Res. 43 (2004) 4864–4870.

[43] S. Fukada, N. Nakamura, J. Monden, M. Nishikawa, Experimental study of cracking methane by Ni/SiO2 catalyst, J. Nucl. Mater. 329–333 (2004) 1365–1369.

[44] U.P.M. Ashik, W.M.A. Wan Daud, H.F. Abbas, Methane decomposition kinetics and reaction rate over Ni/SiO2 nanocatalyst produced through co-precipitation cum modified Stöber method, Int. J. Hydrog. Energy 42 (2017) 938–952.

[45] M.D. Yadav, K. Dasgupta, A.W. Patwardhan, A. Kaushal, J.B. Joshi, Kinetic study of single-walled carbon nanotube synthesis by thermocatalytic decomposition of methane using floating catalyst chemical vapour deposition, Chem. Eng. Sci. 196 (2019) 91–103.

[46] M.D. Yadav, A.W. Patwardhan, J.B. Joshi, K. Dasgupta, Kinetic study of multi-walled carbon nanotube synthesis by thermocatalytic decomposition of methane using floating catalyst chemical vapour deposition, Chem. Eng. J. 377 (2019) 119895.

[47] S. Douven, S.L. Pirard, G. Heyen, D. Toye, J.-P. Pirard, Kinetic study of double-walled carbon nanotube synthesis by catalytic chemical vapour deposition over an Fe-Mo/MgO catalyst using methane as the carbon source, Chem. Eng. J. 175 (2011) 396–407.

[48] S.K. Saraswat, B. Sinha, K.K. Pant, R.B. Gupta, Kinetic study and modeling of homogeneous thermocatalytic decomposition of methane over a Ni–Cu–Zn/Al2O3 catalyst for the production of hydrogen and bamboo-shaped carbon nanotubes, Ind. Eng. Chem. Res. 55 (2016) 11672–11680.

[49] S.G. Zavarukhin, G.G. Kuvshinov, The kinetic model of formation of nanofibrous carbon from CH4–H2 mixture over a high-loaded nickel catalyst with consideration for the catalyst deactivation, Appl. Catal. A: Gen. 272 (2004) 219–227.

[50] M. Borghei, R. Karimzadeh, A. Rashidi, N. Izadi, Kinetics of methane decomposition to COx-free hydrogen and carbon nanofiber over Ni–Cu/MgO catalyst, Int. J. Hydrog. Energy 35 (2010) 9479–9488.

[51] A. Amin, W. Epling, E. Croiset, Reaction and deactivation rates of methane catalytic cracking over nickel, Ind. Eng. Chem. Res. 50 (2011) 12460–12470.

[52] M. Nasir Uddin, W.M.A. Wan Daud, H.F. Abbas, Kinetics and deactivation mechanisms of the thermal decomposition of methane in hydrogen and carbon nanofiber Co-production over Ni-supported Y zeolite-based catalysts, Energy Convers. Manage. 87 (2014) 796–809.

[53] Q. Chen, A.C. Lua, Kinetic reaction and deactivation studies on thermocatalytic decomposition of methane by electroless nickel plating catalyst, Chem. Eng. J. 389 (2020) 124366.

[54] M.C. Demicheli, E.N. Ponzi, O.A. Ferretti, A.A. Yeramian, Kinetics of carbon formation from CH4-H2 mixtures on nickel-alumina catalyst, Chem. Eng. J. 46 (1991) 129–136.

[55] I. Alstrup, M.T. Tavares, Kinetics of carbon formation from CH4 + H2 on silica-supported nickel and Ni-Cu catalysts, J. Catalysis 139 (1993) 513–524.

[56] J.W. Snoeck, G.F. Froment, M. Fowles, Kinetic study of the carbon filament formation by methane cracking on a nickel catalyst, J. Catalysis 169 (1997) 250–262.

[57] G.G. Kuvshinov, Y.I. Mogilnykh, D.G. Kuvshinov, Kinetics of carbon formation from CH4–H2 mixtures over a nickel containing catalyst, Catal. Today 42 (1998) 357–360.

[58] G. Towler, R. Sinnott, In Chemical Engineering Design, third ed., Butterworth-Heinemann, 2022,

[59] J.R. Lattner, Fluid bed methanol synthesis, 2009.

[60] H.S. Fogler, Elements of Chemical Reaction Engineering, Sixth Edition, Global edition, in: Prentice Hall International Series in the Physical and Chemical Engineering Sciences, Pearson, Boston, 2022.

[61] P. Virtanen, et al., SciPy 1.0: Fundamental algorithms for scientific computing in python, Nature Methods 17 (2020) 261–272.

[62] M.L. Abell, J.P. Braselton, In Differential Equations with Mathematica, Fourth ed., Academic Press, Oxford, 2016,

[63] V. Kalman, J. Voigt, C. Jordan, M. Harasek, Hydrogen purification by pressure swing adsorption: High-pressure PSA performance in recovery from seasonal storage, Sustain. 14 (21) (2022) 14037.

[64] V. Kalman, A. Makaruk, E. Engin, A. Balla, M. Harasek, Simulation of hydrogen–methane separation with pressure swing adsorption, in: F. Manenti, G.V. Reklaitis (Eds.), Computer Aided Chemical Engineering, Vol. 53, Elsevier, 2024, pp. 931–936.

[65] S. Sircar, W.E. Waldron, M.B. Rao, M. Anand, Hydrogen production by hybrid SMR–PSA–SSF membrane system, Sep. Purif. Technol. 17 (1999) 11–20.

[66] S. Reddy, S. Vyas, Recovery of carbon dioxide and hydrogen from PSA tail gas, Energy Procedia 1 (2009) 149–154.

[67] I. Sharma, D. Friedrich, T. Golden, S. Brandani, Exploring the opportunities for carbon capture in modular, small-scale steam methane reforming: An energetic perspective, Int. J. Hydrog. Energy 44 (2019) 14732–14743.

[68] I. Burgers, L. Dehdari, P. Xiao, K.G. Li, E. Goetheer, P. Webley, Techno-economic analysis of PSA separation for hydrogen/natural gas mixtures at hydrogen refuelling stations, Int. J. Hydrog. Energy 47 (2022) 36163–36174.

[69] I.D. Rahatwan, P.P.D.K. Wulan, M. Solahudin, Techno-economic analysis of pilot scale carbon nanotube production from LPG with Fe-Co-Mo/MgO catalyst in Indonesia, AIP Conf. Proc. 2230 (2020) 030013.

[70] P.X. Hou, S. Bai, Q.H. Yang, C. Liu, H.M. Cheng, Multi-step purification of carbon nanotubes, Carbon 40 (2002) 81–85.

[71] A.R. Harutyunyan, B.K. Pradhan, J. Chang, G. Chen, P.C. Eklund, Purification of single-wall carbon nanotubes by selective microwave heating of catalyst particles, J. Phys. Chem. B 106 (2002) 8671–8675.

[72] I.W. Chiang, B.E. Brinson, R.E. Smalley, J.L. Margrave, R.H. Hauge, Purification and characterization of single-wall carbon nanotubes, J. Phys. Chem. B 105 (2001) 1157–1161.

[73] I.W. Chiang, B.E. Brinson, A.Y. Huang, P.A. Willis, M.J. Bronikowski, J.L. Margrave, R.E. Smalley, R.H. Hauge, Purification and characterization of single-wall carbon nanotubes (SWNTs) obtained from the gas-phase decomposition of CO (HiPco process), J. Phys. Chem. B 105 (2001) 8297–8301.

[74] A.E. Agboola, R.W. Pike, T.A. Hertwig, H.H. Lou, Conceptual design of carbon nanotube processes, Clean Technol. Environ. Policy 9 (2007) 289–311.

[75] I.-W. Wang, A.R. Dagle, T. Suvra Khan, A.J. Lopez-Ruiz, L. Kovarik, Y. Jiang, M. Xu, Y. Wang, C. Jiang, D.S. Davidson, P. Tavadze, L. Li, J. Hu, Catalytic decomposition of methane into hydrogen and high-value carbons: combined experimental and DFT computational study, Catal. Sci. Technol. 11 (2021) 4911–4921.

[76] C. Jiang, et al., Methane catalytic pyrolysis by microwave and thermal heating over carbon nanotube-supported catalysts: Productivity, kinetics, and energy efficiency, Ind. Eng. Chem. Res. 61 (2022) 5080–5092.

[77] J. Ding, C. Yan, Y. He, C. Wang, Supercritical CO2 sequestration and enhanced gas recovery in tight gas reservoirs: Feasibility and factors that influence efficiency, Int. J. Greenh. Gas Control. 105 (2021) 103234.

[78] D.-Y. Peng, D.B. Robinson, A new two-constant equation of state, Ind. Eng. Chem. Fundam. 15 (1976) 59–64.

[79] S.Y.W. Chai, F.J.F. Phang, L.S. Yeo, L.H. Ngu, B.S. How, Future era of techno-economic analysis: Insights from review, Front. Sustain. 3 (2022) 1–22.

[80] J.R. Couper, Process Engineering Economics, CRC Press, Boca Raton, 2003.

[81] R. Turton, Analysis, Synthesis, and Design of Chemical Processes, fourth ed., in: Prentice-Hall International Series in the Physical and Chemical Engineering Sciences, Prentice Hall, Upper Saddle River, NJ, 2012.

[82] Hourly mean wage for chemical plant and system operators in chemical manufacturing in the United States, 2023, https://www.bls.gov/oes/2023/may/oes518091.htm.

[83] O. Tang, J. Rehme, P. Cerin, Levelized cost of hydrogen for refueling stations with solar PV and wind in Sweden: On-grid or off-grid? Energy 241 (2022) 122906.

[84] K.M. Van Allsburg, F.G. Baddour, L. Snowden-Swan, CatCost, 2021, https://catcost.chemcatbio.org/.

[85] A. Misra, J.R. Raney, A.E. Craig, C. Daraio, Effect of density variation and non-covalent functionalization on the compressive behavior of carbon nanotube arrays, Nanotechnol. 22 (2011) 425705.

[86] Natural gas EU Dutch TTF, 2024, https://tradingeconomics.com/commodity/eu-natural-gas, (Accessed 14 April 2025).

[87] A. Mengden, Carbon taxes in Europe, 2024, https://taxfoundation.org/data/all/eu/carbon-taxes-europe-2024/, (Accessed 14 April 2025).

[88] Electricity prices in Netherlands, 2025, https://euenergy.live/country.php?a2=NL, (Accessed 14 April 2025).

[89] International Energy Agency (IEA) Northwest European hydrogen monitor 2024, 2024, https://www.iea.org/reports/northwest-european-hydrogen-monitor-2024, Place: Paris.

[90] Ember, E. Institute, Carbon intensity of electricity generation – Ember and Energy Institute, 2024, https://ourworldindata.org/grapher/carbon-intensity-electricity, Published: Dataset. (Accessed 5 March 2025).

[91] N. Metropolis, S. Ulam, The Monte Carlo method, J. Amer. Statist. Assoc. (1949).

[92] Agency (IEA), I. E. CCUS policies and business models: Building a commercial market, 2023, https://www.iea.org/reports/ccus-policies-and-business-models-building-a-commercial-market, Place: Paris.

[93] B. Parkinson, P. Balcombe, J.F. Speirs, A.D. Hawkes, K. Hellgardt, Levelized cost of CO2 mitigation from hydrogen production routes, Energy Environ. Sci. 12 (2019) 19–40.

[94] S.E. Schoemaker, T.A.J. Welling, D.F.L. Wezendonk, B.H. Reesink, A.P. van Bavel, P.E. de Jongh, Carbon nanofiber growth from methane over carbon-supported NiCu catalysts: Two temperature regimes, Catal. Today 418 (2023) 114110.